Faculty of Medicine and Life Sciences
School for Life Sciences

Master of Biomedical Sciences

Master's thesis

Elucidating the role of phosphodiesterase 4B in microglial activity and microglia-mediated synaptic elimination during Alzheimers disease

Femke Mussen

Thesis presented in fulfillment of the requirements for the degree of Master of Biomedical Sciences, specialization Molecular Mechanisms in Health and Disease

SUPERVISOR :

Prof. dr. Tim VANMIERLO

MENTOR :

De heer Ben ROMBAUT

Transnational University Limburg is a unique collaboration of two universities in two countries: the University of Hasselt and Maastricht University.

2022
2023

Faculty of Medicine and Life Sciences
School for Life Sciences
Master of Biomedical Sciences

Master's thesis

Elucidating the role of phosphodiesterase 4B in microglial activity and microglia-mediated synaptic elimination during Alzheimers disease

Femke Mussen
Thesis presented in fulfillment of the requirements for the degree of Master of Biomedical Sciences, specialization Molecular Mechanisms in Health and Disease

SUPERVISOR :
Prof. dr. Tim VANMIERLO

MENTOR :
De heer Ben ROMBAUT

Elucidating the role of phosphodiesterase 4B in microglial activity and microglia-mediated synaptic elimination in Alzheimer's disease

Femke Mussen[1,2], Lisa Koole[2,3], Ben Rombaut[1, 2, 3, 4], Tim Vanmierlo[1, 2, 3, 4]

[1] University Hasselt, Campus Diepenbeek, Agoralaan building D, 3590 Diepenbeek
[2]Department of Neuroscience, Biomedical Research Institute BIOMED, Hasselt University, 3590 Diepenbeek, Belgium.
[3]Department of Psychiatry and Neuropsychology, School for Mental Health and Neuroscience, Maastricht University, 6229ER Maastricht, The Netherlands.
[4]University MS Center (UMSC) Hasselt-Pelt, Hasselt University, 3500 Hasselt, Belgium.

Running title: The role of Pde4b in microglial activity

To whom correspondence should be addressed: Tim Vanmierlo, Tel: +32 11 26 92 28; Email: tim.vanmierlo@uhasselt.be

ABSTRACT

Alzheimer's disease (AD) is characterized by prominent cognitive decline, but no treatments currently slow disease progression. Excessive synaptic elimination by microglia is correlated with the degree of cognitive decline in AD patients. Elevating cAMP levels by inhibiting phosphodiesterase 4 (PDE4) has already been demonstrated to lower microglia reactivity and decrease cognitive decline in rodent models. However, PDE4 inhibition coincides with severe side effects leading to restricted clinical translation. The PDE4 subtype PDE4B inhibition was demonstrated to lower microglia activation and circumvent the emetic side effects. Therefore, the effect of microglia-specific PDE4B modulation on synaptic elimination in AD was elucidated. The effect of PDE4 subtype inhibition was investigated on primary murine microglia morphology. The phagocytic capacity of pHrodo-labeled synaptosomes in different *Pde4b* murine microglia genotypes was used to elucidate the role of *Pde4b* on synaptic elimination. Lastly, a bone marrow transplantation was used to unravel the role of the phagocyte-specific expression of *Pde4b* on cognitive decline in a rodent model of AD. PDE4D and PDE4B inhibition decreased microglial complexity and improved motility, respectively. Heterozygous deficiency of *Pde4b* revealed to improve phagocytosis, but compensatory mechanisms to regulate cAMP were indicated. The effect of phagocyte-specific *Pde4b* expression in the CNS on cognition could not be determined due to the unexpected death of the AD chimeras, hypothesized through radiation-induced injury. In conclusion, *Pde4b* in microglia showed to play a crucial role in morphology and phagocytosis, but the *Pde4b*-specific effect on microglia in modulating excessive synaptic elimination in AD remains to be elucidated.

INTRODUCTION

Currently, 55 million elderly are suffering from Alzheimer's disease (AD). This progressive neurodegenerative disorder is characterized by notable memory deficits and problems in the execution of daily tasks in early and moderate AD. In the later stages of AD, the disease will evolve toward severe cognitive impairment and the need for continuous nursing (1). Additionally, AD is the predominant form of dementia, which is the seventh leading cause of death worldwide (2). Consequently, tremendous efforts have been made to treat cognitive decline in AD. The current medications for mild to moderate AD include the cholinesterase inhibitors donepezil, rivastigmine, and galantamine. In addition, N-methyl D-aspartate (NMDA) receptor agonist memantine is used to lower disease symptoms in late AD. The available therapies only work symptomatically since disease progression is not ceased, leading to further neurodegeneration and impaired quality of life (3). Past research focused on targeting AD's pathological hallmarks, specifically, the accumulation of extracellular amyloid beta (Aβ) plaques and the hyperphosphorylation of tau forming neurofibrillary tangles inside neurons. Although some medications could reduce Aβ accumulation or tau hyperphosphorylation in

human clinical trials, these therapies failed to improve cognition in humans (4). Hence, novel therapeutic approaches are necessary to improve cognitive function in AD and hamper disease progression.

Excessive synaptic elimination is observed early in AD, and the degree of cognitive decline is correlated with the amount of synaptic elimination in AD patients (5, 6). Synapses allow communication between neurons. Maintaining synaptic homeostasis is crucial for the physiological functioning of the central nervous system (CNS). Synapses are classified as electrical and chemical synapses, whereby the latter is the predominant type in the mammalian CNS. Furthermore, chemical synapses have a high diversity based on the cellular contact location between the pre- and postsynaptic neuron, the used neurotransmitter, and the effect of these neurotransmitters on the postsynaptic membrane. The effect of neurotransmitter release on the postsynaptic membrane can be either excitatory or inhibitory. The human CNS's primary excitatory and inhibitory neurotransmitters are glutamate and gamma-aminobutyric acid (GABA), respectively (7). Additionally, excitatory synapses are mainly formed between dendritic spines, which are small protrusions of the postsynaptic dendritic shaft. In contrast, inhibitory synapses are predominantly formed directly on the dendritic shaft (8).

Synaptic signaling and number are plastic. The number of synapses is dynamic as there is a constant turnover regulated in an activity-dependent manner. As such, low levels of synaptic activity will result in long-term depression and the loss of dendritic spines (7). Besides synaptic activity, glial cells, especially microglia, have been shown to be important regulators of synaptic plasticity and homeostasis in the healthy and diseased CNS (9).

Microglia are the resident immune cells of the CNS and show remarkable plasticity in both morphology and function to counteract changes in the environment of the brain and spinal cord. Microglia originate from the yolk sac and enter the CNS via developing blood vessels, where they will adopt an amoebic phenotype (10). Research showed that these embryonic, amoebic microglia promote synaptogenesis via the secretion of growth factors (11, 12). In contrast, microglial phagocytosis eliminates weak and excessive synapses in the process of synaptic pruning to maintain a balance in synaptic number (13). Synaptic elimination of weak or excessive synapses is suggested to be regulated by the complement system. More specifically, complement system components such as C1q and C5a tag redundant synapses, leading to microglial phagocytosis (14). Additionally, triggering receptor expressed on myeloid cell (*Trem2*) deficiencies reduce the phagocytosis of redundant synapses and are suggested as an important mediator of microglial phagocytosis (15). Therefore, research showed that microglia have an essential role in sustaining the balance of synaptic density during development. Although synaptogenesis and synaptic pruning are less prevalent in the adult CNS, their balance is crucial to maintaining CNS health in adulthood.

In the adult CNS, microglia will adopt a ramified phenotype with filopodia and continuously protrude and retract their multiple long branches to surveil the CNS environment (16). These microglial ramifications have been shown to contact dendritic spines and synapses. Interestingly, microglia preferentially contact active neurons, often followed by a transient growth in dendritic spines (17, 18). Upon encountering weak or excessive synapses, microglia will shift to an amoebic phenotype characterized by a round cell body and short protrusions. Subsequently, amoebic microglia migrate toward the synapse, followed by microglial activation and synaptic phagocytosis (9, 19). Furthermore, inflammatory products, including tumor necrosis factor-alpha (TNF-α), interleukin-1 beta (IL-1β), and nitric oxide (NO) will be released from microglia. Both TNF-α and IL-1β influence synaptic plasticity by reducing long-term potentiation, resulting in decreased synaptic strength. Besides regulating synaptic plasticity, microglia have already been demonstrated to be key regulators in controlling the number and function of excitatory synapses in the adult CNS (20, 21). Accumulating data provides evidence that microglia are crucial in maintaining synaptic homeostasis and regulating synaptic plasticity in the healthy adult CNS (9). Nevertheless, microglia also contribute to excessive synaptic elimination in AD, leading to imbalances of synaptic homeostasis, which is correlated with cognitive decline in AD patients (9, 22, 23). In particular, excitatory synapses are reduced concurrent with a decrease in dendritic spines in the brain of AD patients. Consequently, influencing microglial activity during AD can be a promising strategy to reclaim synaptic homeostasis in the CNS and improve cognitive function in AD.

The second messenger 3'5'-cyclic adenosine monophosphate (cAMP) is an important regulator for microglial surveillance and motility (8, 24). Increasing cAMP levels reduces the production of pro-inflammatory cytokines and enhances anti-inflammatory cytokine production by microglia (25, 26). Additionally, cAMP signaling and its downstream molecule cAMP response element-binding protein (CREB) has been shown to be essential for cognitive function (27, 28). Hence, balanced cAMP levels are necessary to have a proper physiological functioning of the cells in the CNS. Therefore, targeting cAMP in a spatiotemporal manner is promising to reclaim synaptic balances in AD. cAMP is produced from AMP by adenylyl cyclase, while phosphodiesterase (PDE) is responsible for cAMP breakdown by hydrolysis. PDEs can be divided into 11 (PDE1-11) gene families based on the protein structure. Furthermore, each PDE gene family will have substrate specificity for either cAMP (PDE4, 7, and 8), or cGMP (PDE5, 6, and 9), or have dual substrate specificity (PDE1, 2, 3, 10, and 11). The gene families contain 21 genes (e.g., PDE4B) and encode even more isoforms by alternative splicing (e.g., PDE4B1) (29). PDEs show cell-specific expression that can be influenced during diseases (30). In the CNS, the PDE4 gene family is highly expressed. Inhibition of PDE4 showed to have a neuroprotective and anti-inflammatory effect *in vivo* (31). Additionally, PDE4 inhibition improved cognitive function in mouse models of AD (32-35). The PDE4 genes influence microglial characteristics such as inflammatory phenotype and motility (26, 30). Consequently, PDE4 inhibition was suggested as a promising therapeutic target to decrease cognitive decline in AD patients. Unfortunately, PDE4 inhibition has been demonstrated to have side effects, such as nausea and headaches, preventing its clinical translation (36). PDE4B is a gene in the PDE4 family and its inhibition was demonstrated to avoid emesis in rodent models (37). PDE4B consists of five isoforms (PDE4B1-5) that are highly expressed in human microglia. PDE4B1, 3, and 4 contain upstream conserved regions (UCR) 1 and 2 and are, therefore, considered long isoforms. In contrast, PDE4B2 and PDE4B5 contain only UCR 2 or truncated UCR 2, respectively. Consequently, PDE4B2 is described as the short isoform, while PDE4B5 is the super-short isoform (38). PDE4B is acutely upregulated in microglia and macrophages during traumatic brain injury and spinal cord injury (39, 40).

Interestingly, the upregulation of PDE4B coincides with the elevation of the inflammatory markers TNF-α and IL-1β (40). Inhibiting PDE4B *in vitro* or *Pde4b* ablation *in vivo* reduced the production of inflammatory cytokines (40, 41). Consequently, PDE4B is considered as a crucial regulator of microglial immune function. Therefore, PDE4B modulation has been shown to be a promising strategy to modulate microglia function in neurodegenerative disorders, such as AD, without causing the emetic side effects observed during general PDE4 inhibition. Although the immunomodulatory properties of PDE4B inhibition on microglia are described, the influence of PDE4B modulation to regulate microglial phagocytosis is unknown.

Therefore, this project will elucidate the role of *Pde4b* in microglia-mediated excessive synaptic elimination in AD. Firstly, the effect of PDE4-subtype inhibition on microglial morphology will be investigated since microglia morphology is correlated with its function (42). Secondly, the role of *Pde4b* expression on microglia-mediated synaptic elimination will be elucidated *in vitro* using pHrodo-labeled synaptosomes. Lastly, the effect of phagocyte-specific *Pde4b* expression on cognitive decline in AD will be unraveled in a rodent model with phagocyte-specific *Pde4b* expression. In this way, more insights will be gained into the underlying mechanisms of the *Pde4b* modulatory effect on microglia during AD.

EXPERIMENTAL PROCEDURES

Animals – Post-natal three to five (P0-P5) days-old C57BL/6 mice with wild type ($Pde4b^{+/+}$), heterozygous ($Pde4b^{+/-}$), or homozygous-deficient ($Pde4b^{-/-}$) expression of *Pde4b* were used for circularity, phagocytosis, and qPCR experiments. To investigate the influence of PDE4(B) inhibition on microglial surveillance, P21 C57BL/6 mice with heterozygous expression of enhanced green fluorescent protein (eGFP) under the control of microglia-specific C-X-C chemokine receptor 1 ($Cx3cr1^{eGFP/+}$) were used. Lastly, female APPswePS1ΔE9 (APP/PS1) were subjected to a bone marrow transplantation (BMT) to investigate the phagocyte-specific effect of *Pde4b* expression on cognition. All animals were housed with *ad libitum* access to water and food in the BIOMED research facility. APP/PS1 mice were housed in a reversed 12 h light/dark cycle while the other animals were accommodated in a 12 h light/dark cycle. All animal experiments

were conducted in accordance with the European Community guiding principles on the care and use of animals and were approved by the local Ethical Committee of Hasselt University.

Primary microglia isolation – Primary murine microglia were isolated using the shake-off method for circularity, phagocytosis, and qPCR experiments as previously described (Supplementary information) (37). Microglia used for surveillance experiments were isolated from the cortices of P21 $Cx3cr1^{eGFP/+}$ mice by magnetic activated cell-sorting (MACS), as described by Bohlen *et al.* (Supplementary information) (43).

Microglial circularity – $Pde4b^{+/+}$ primary murine microglia were seeded at a density of 30 000 cells/well in a poly-L-lysine (PLL; 50 µg/mL, 25988-63-0, Sigma-Aldrich) pre-coated 24-well plate (83.3922, Sarstedt) and incubated with PDE4 inhibitor roflumilast (3 nM/well,) (IC_{50} PDE4: 0.2-1 nM), PDE4B inhibitor A33 (100 nM/well; 915082-52-9, Sigma-Aldrich) (IC_{50} PDE4B: 27 nM), a PDE4D inhibitor (100 nM/well) (IC_{50} PDE4D: 30 nM), or vehicle (dimethyl sulfoxide, DMSO, 1:1000; 67-68-5, VWR Prolabo) to investigate the effect of PDE4(B/D) inhibition on microglia morphology. Images were made 0, 15, 45, and 360 min after the addition of the inhibitors with the Incucyte® S3 Live-Cell Analysis System (Essen Bioscience) and analyzed using Fiji (ImageJ v2.0, Open source software) by manually defining cell contours and quantifying shape parameters. The circularity was calculated by $4\pi(\text{area/perimeter}^2)$.

Microglial surveillance – Primary murine $Cx3cr1^{eGFP/+}$ microglia were seeded on collagen (2µg/mL; 9007-34-5, Sigma-Aldrich) and Poly-D-Lysine (PDL; A38904-01, Gibco) pre-coated glass inserts (80826, Ibidi) at a density of 30 000 cells/well. The culture medium was replaced by Krebs solution (pH 7.4, 150 mM NaCl, 6 mM KCl, 1.5 mM $CaCl_2$, 1 mM $MgCl_2$, 10 mM HEPES, and 10 mM glucose monohydrate) before imaging with the Zeiss LSM880 confocal microscope. Filopodia motility was obtained during a time series before and after the administration of 3 nM roflumilast, 100 nM A33, or vehicle (0.05% DMSO). The images were acquired using a 63x oil immersion objective and the airyscan detector. The surveilled area was determined by measuring the area covered by filopodia in a defined region of interest with Fiji.

Filopodia length and number were quantified with the segmented line tool in Fiji.

Synaptosome phagocytosis – Synaptosomes were isolated from the brains of adult $Pde4b^{+/+}$ mice, followed by mechanical homogenization with the Dounce homogenizer in Syn-PER™ Synaptic Protein Extraction Reagent (87793, ThermoFisher Scientific) supplemented with a protease (05892970001, Roche) and a phosphatase (04906837001, Roche) inhibitor. Next, the synaptosomes were labeled with pHrodo dye (P3660, Invitrogen ThermoFisher) according to the manufacturer's instructions. $Pde4b^{+/+}$, $Pde4b^{+/-}$, or $Pde4b^{-/-}$ primary murine microglia were cultured on a PLL pre-coated 24-well plate and seeded at a density of 200 000 cells/well. The synaptosomes were removed after 40 min. Images were obtained every 30 min, for 24 h, starting directly after the administration of the pHrodo-labeled synaptosomes with the Incucyte® S3 Live-Cell Analysis System. Images were processed using Fiji, and the area covered by pHrodo-positive cells, total cell area, and mean gray intensity were calculated. Afterward, the phagocytic index was calculated by dividing the pHrodo-positive area by the total cell area. The amplitude in intensity was calculated by subtracting the minimum gray value from the maximum gray value at 2-6 h (peak) and was normalized by the minimum gray value.

qPCR – qPCR was performed according to an in-house method for phagocytosis genes *Trem2*, cluster of differentiation (*Cd36*), and toll-like receptor 4 (*Tlr4*). The gene expression of other *Pde* genes *Pde4a*, *Pde7a*, *Pde7b*, and *Pde8a* were assessed (Supplementary information).

Bone marrow transplantation APP/PS1 mice – Recipient 6 weeks-old female APP/PS1 mice (3 groups with n=16/group) or WT mice (n=16) were pre-treated for seven days with polymyxin B sulfate salt (1:1000; P4932-5MU, Sigma) and neomycin (1:1000; 21810031, Gibco) added to the drinking water before being irradiated with 8 Gy to ablate endogenous bone marrow cells. Next, bone marrow cells from 10-week-old $Pde4b^{+/+}$, $Pde4b^{+/-}$, or $Pde4b^{-/-}$ mice were obtained by flushing the femur with DMEM 10:1. Five million bone marrow cells were intravenously injected into the tail vein of xylazine (10 mg/kg) ketamine (80 mg/kg) anesthetized APP/PS1 recipient mice, rendering four unique groups (**Table 1**). Subsequently,

APP/PS1 or WT mice were given 6 weeks of antibiotics containing polymyxin and neomycin. The colony-stimulating factor 1 receptor (CSF-1R) inhibitor PLX5622 (C-1521, Chemgood) was added to the food and given for 14 days *ad libitum*, starting one week after BMT, to deplete CNS microglia. Subsequently, bone marrow-derived phagocytes, resembling microglia, repopulated the CNS rendering phagocyte-specific expression of *Pde4b* in the CNS. Cognitive tests were performed at baseline (6 months of age). The animals were single-housed one week before cognitive tests. An echocardiography was made in a new cohort (Supplementary information).

Table 1: BMT groups. The recipient mice were either APP/PS1 (AD) mice or WT mice. The donor mice had WT (*Pde4b$^{+/+}$*), heterozygous (*Pde4b$^{+/-}$*), or no (*Pde4b$^{-/-}$*) *Pde4b* expression. n=16 per group

Genotype recipient	WT	AD	AD	AD
Genotype donor	Pde4b $^{+/+}$	Pde4b $^{+/+}$	Pde4b $^{+/-}$	Pde4b $^{-/-}$

BMT, Bone marrow transplantation; AD, Alzheimer's disease; WT, Wild-type.

Cognitive tests – The object location task (OLT) was used to assess spatial memory in APP/PS1 mice with phagocyte-specific expression of *Pde4b* (**Table 1**). The OLT was performed as previously described (44). Briefly, the exploration time of each object in trial 1 (T1) (with identical, symmetrically placed objects) and in trial 2 (T2) (with one moved and one stationary object) was recorded. Next, the discrimination index (D2) was calculated for T2 according to the following formula: D2= [(exploration time moved object)-(exploration time for the stationary object)]/(total exploration time in T2). Additionally, the spontaneous Y-maze alternation task was used to determine working memory in APP/PS1 chimeras (**Table 1**). The mouse was left free to explore the Y-maze for 6 min. Next, the working memory was calculated by defining the percentage of alternations calculated by the following formula: [number of triads/(total number of entries-2)]*100. A triad is considered the sequential entrance of three different arms. All cognitive experiments were executed by a blinded person for the experimental groups. Additional information regarding the procedure, training days, and randomization can be found in the Supplementary information.

Statistics – GraphPad Prism 9 (GraphPad Software Inc) was used for the analysis and representation of the figures. Outliers were detected and excluded using the ROUT outlier test. Normality and equal distribution of variances were tested using the Shapiro-Wilk and Brown-Forsythe tests, respectively. Comparisons between (un)paired groups were performed with a (un)paired t-test or Wilcoxon test. A one-way ANOVA, Kruskal-Wallis test, or Welsh ANOVA with a Tukey's test or Dunn's test for multiple comparisons was used to compare more than two groups. A two-way ANOVA or Friedmann's test with Šídák's multiple comparisons test or Dunn's correction, respectively was conducted to detect differences between groups over time or between treatments. Differences from zero or 50% for the OLT and Y-maze were determined using a one-sample t-test. The survival curve was generated with a Kaplan-Meier analysis with a Logrank test to detect differences in survival probability between the different groups, corrected for multiple comparisons with the Bonferroni correction. Data are represented as mean ± SEM.

RESULTS

Acute PDE4 inhibition increased microglial circularity – Microglia morphology is strongly correlated with microglia function (42). Therefore, we investigated the effect of PDE4, PDE4B, and PDE4D inhibition on primary murine microglia morphology. The microglia were incubated with DMSO, PDE4 inhibitor roflumilast, PDE4B inhibitor A33, or a PDE4D inhibitor and circularity was measured after 0, 15, 45, or 360 min of incubation. A low circularity value indicates a high degree of ramifications. There were no differences over time in microglial circularity during 0.05% DMSO incubation. PDE4 inhibition with 3 nM roflumilast significantly (***p<0.001) decreased microglial complexity after 45 min of incubation, reflected by an increase in circularity value. In contrast, PDE4B inhibition with 100 nM of A33 did not alter microglia morphology over time. Lastly, PDE4D inhibition showed a trend to increase microglia circularity over time, starting 15 min after incubation (**Figure 1**). Subsequently, PDE4D inhibition demonstrated to have a trend to decrease microglia complexity further after 45 and 360 min of incubation compared to 15 min incubation (**Figure 1**).

PDE4(B) inhibition showed a trend to increase microglial surveillance – Microglia

continuously survey the microenvironment by repeated extraction and retraction of their filopodia in physiological conditions (10). However, microglia in neurodegenerative disorders are characterized by shorter ramifications and fewer filopodia, leading to compromised surveillance of the CNS environment (45). To elucidate the effect of PDE4(B) on microglial surveillance, filopodia motility was measured during live cell imaging and filopodia movement at baseline was compared with acute inhibition of PDE4(B) in cultured, primary murine *Cx3cr1*$^{eGFP/+}$ microglia. Normally, highly branched microglia are obtained during TIC incubation for seven days. However, our experiments could not acquire high-order branched microglia (**Supplementary Figure 1**). Therefore, filopodia movement was quantified from the lamellipodia, lower-degree branches, or cell body. Representative color-coded pictures of cell areas with filopodia movement at baseline and during treatment with DMSO (**Figure 2.A**), roflumilast (**Figure 2.C**), or A33 (**Figure 1.E**) are shown. After 3 min of treatment with 0.05% DMSO, no significant change in the scanned area (**Figure 2.A, B, G**), nor number (**Figure 2.H**), and length (**Figure 2.I**) of filopodia was observed. In contrast, 3 min of incubation with 3 nM of PDE4 inhibitor roflumilast showed an increasing trend in filopodia surveillance (**Figure 2.C,D**), which was further demonstrated by an increased difference of surveilled area between baseline and treatment in the roflumilast treated group (**Figure 2.G**), and the number of filopodia (**Figure 2.H**). Despite this, the length of filopodia did not alter when the cells were treated with 3 nM of roflumilast (**Figure 2.I**). Lastly, 100 nM of PDE4B inhibitor A33 indicated an increased trend in the surveilled filopodia area (**Figure 2.E, F**). The difference in surveilled area between the baseline and treated condition did not reveal a significant difference and showed limited changes compared to the DMSO group (**Figure 2.G**). Although the number of filopodia indicated a trend toward increased number (**Figure 2.H**), the filopodia length upon A33 treatment was significantly reduced ($p < 0.05$) (**Figure 2.I**)
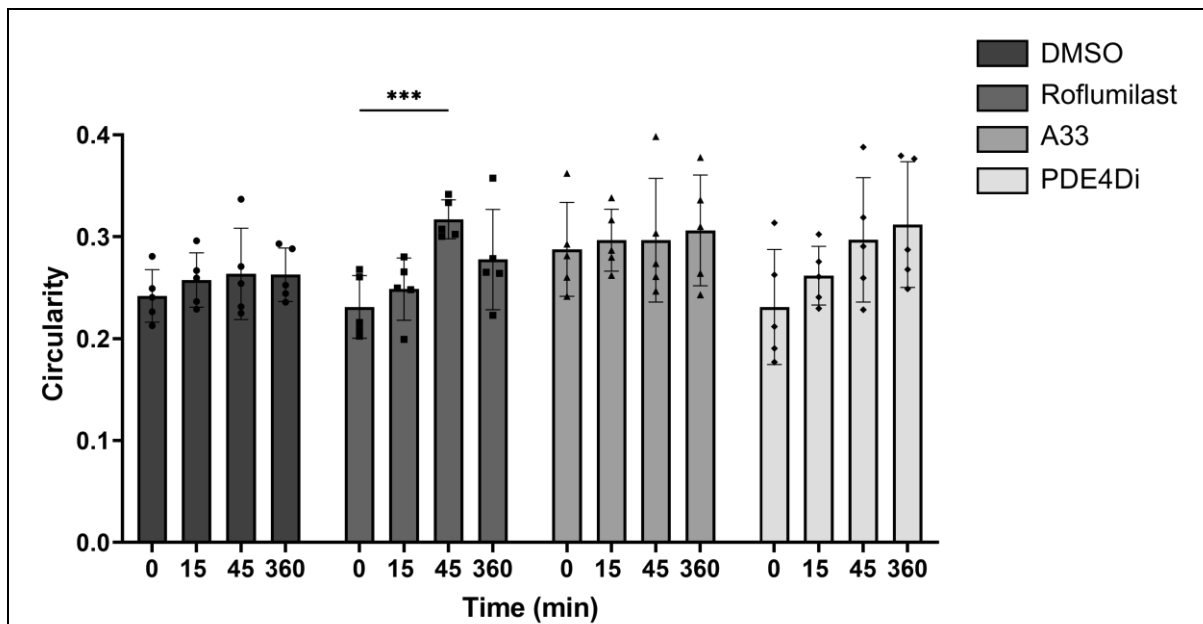

Figure 1: Acute PDE4 inhibition increased microglial circularity after 45 min of incubation. Circularity measurements of cultured primary murine microglia after 0, 15, 45, or 360 min of incubation with 0.05% DMSO, 3 nM roflumilast, 100 nM of A33, or 100 nM of a PDE4D inhibitor. Data are represented as mean ± SEM. Data were analyzed with a two-way ANOVA with Šídák's multiple comparisons test. ***p<0.001, n=5 images per condition with 15 cells traced per image. DMSO, Dimethyl sulfoxide; PDE4Di, PDE4D inhibitor.
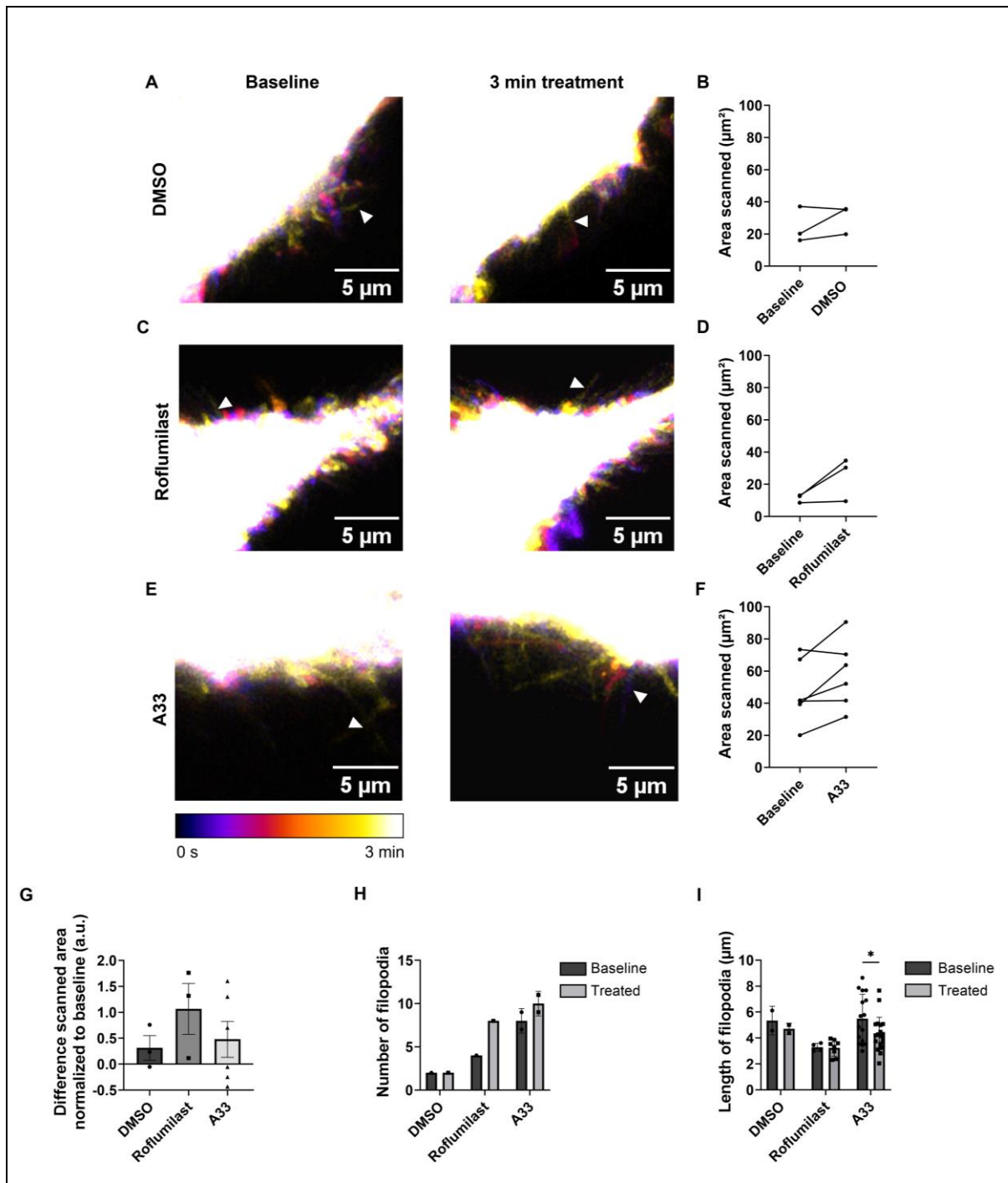
Figure 2: Acute inhibition of PDE4(B) showed an increasing trend for microglial surveillance. (A, C, and E) Representative temporal color coded overlay pictures of microglia during baseline or after 3 min of treatment with (A) 0.05% DMSO, (C) 3 nM roflumilast, or (E) 100 nM A33 with the white arrowhead indicating filopodia. The color-coded bar represents the change in color over time, a scale bar of 5 µm was used. (B, D, and F) Scanned area (µm²) of filopodia with each dot representing a single region of a cell at baseline or after 3 min of treatment with (B) 0.05% DMSO (n=3 regions, 1 cell), (D) 3 nM roflumilast (n=3 regions, 1 cell) or (F) 100 nM A33 (n=6 regions, 2 cells). (G) The difference in the scanned area during treatment and baseline was normalized to the surveilled area at baseline. (H) The number and (I) length (µm) of filopodia were manually measured with Fiji before (baseline) and after 3 min of treatment with DMSO, roflumilast, or A33. Data are represented as mean ± SEM. (G-I) The same regions as with the scanned area were used to determine the number and length of filopodia. Data were analyzed with a (B, D, and F) paired Wilcoxon test, (G) one-way ANOVA with a Tukey's test for multiple comparisons, and (H-I) Friedmann test with Dunn's correction for multiple comparisons, *p<0.05. DMSO, Dimethyl sulfoxide; a.u., arbitrary unit.

7

Pde4b expression influenced phagocytic behavior and gene expression of phagocytosis genes in microglia – Excessive synaptic elimination is correlated with the degree of cognitive decline in AD. Microglia mediate synaptic elimination and, therefore, are a promising target to cease excessive synaptic elimination in AD. The effect of PDE4B on microglia-mediated synaptic elimination was untangled by measuring the phagocytic capacity of pHrodo-labeled synaptosomes by $Pde4b^{+/+}$, $Pde4b^{+/-}$, or $Pde4b^{-/-}$ primary murine microglia. The pH-sensitive pHrodo dye emits red fluorescent light in an acidic environment. Therefore, a red fluorescent signal is only observed when the pHrodo-labeled synaptosomes are phagocytosed by microglia. A lower red fluorescent signal at 3.5 h after pHrodo-labeled synaptosome administration was observed in $Pde4b^{+/+}$ microglia (**Figure 3.A**) compared to $Pde4b^{+/-}$ (**Figure 3.B**), or $Pde4b^{-/-}$ (**Figure 3.C**) microglia indicating less phagocytosis by $Pde4b^{+/+}$ microglia. Indeed, a significantly (***p<0.001) lower phagocytic index, defined as the pHrodo area divided by the cell area, was observed in $Pde4b^{+/+}$ microglia compared to $Pde4b^{+/-}$ microglia from 1 h until 24 h after synaptosome administration (**Figure 3.D**). In addition, $Pde4b^{-/-}$ microglia were revealed to have a significant (*p<0.05) higher phagocytic index in the peak hours of phagocytosis (2-3.5 h) and 24 h after synaptosome administration compared to $Pde4b^{+/+}$ microglia (**Figure 3.D**). The total cell area did not differ between the different groups (**Supplementary Figure 3**). The area under the curve (AUC) also indicated the increased amount of microglia that are phagocytosing in the $Pde4^{+/-}$ (**p<0.01) and $Pde4b^{-/-}$ (*p<0.05) condition than $Pde4b^{+/+}$ microglia (**Figure 3.E**). Additionally, $Pde4b^{+/-}$ microglia showed an elevated phagocytic capacity indicated by a significantly increased amplitude in red intensity between 2-6 h after synaptosome administration than $Pde4b^{+/+}$ microglia (**p<0.01) and $Pde4b^{-/-}$ microglia (*p<0.05) (**Figure 3.F**). There was no difference in phagocytic capacity between $Pde4b^{+/+}$ and $Pde4b^{-/-}$ microglia (**Figure 3.F**). The gene expression of phagocytosis-associated genes *Trem2*, Cluster of differentiation 36 (*Cd36*), and Toll-like receptor 4 (*Tlr4*) were measured to untangle altered phagocytosis regulation during differential expression of *Pde4b* in murine microglia (15, 46). *Trem2*, involved in synaptic phagocytosis, did not differ between the different *Pde4b* microglia groups but showed a trend

toward higher expression in $Pde4b^{+/-}$ microglia (**Figure 3.G**). In contrast, *Cd36* is associated with promoting Aβ clearance and was significantly (**p<0.01) lower expressed in $Pde4b^{+/-}$ microglia compared to $Pde4b^{-/-}$ microglia (**Figure 3.H**). Lastly, *Tlr4* expression showed an increasing trend in expression in $Pde4b^{+/-}$ microglia and a significantly higher expression (*p<0.05) in $Pde4b^{-/-}$ microglia (**Figure 3.I**). Therefore, the differential expression of *Pde4b* influences the gene expression of phagocytosis genes.

Microglia with altered Pde4b expression have modified expression of other cAMP-specific Pde genes – To elucidate if compensatory mechanisms were present in $Pde4b^{+/-}$ or $Pde4b^{-/-}$ microglia, the gene expression of other cAMP-specific PDEs were measured in primary murine microglia with $Pde4b^{+/+}$, $Pde4b^{+/-}$, or $Pde4b^{-/-}$ expression. *Pde4a* expression demonstrated a decreasing trend in gene expression in $Pde4b^{+/-}$ and significantly reduced (***p<0.001) expression in $Pde4b^{-/-}$ microglia (**Figure 4.A**). *Pde7a* showed a significant increase in gene expression compared to $Pde4b^{+/+}$ (*p<0.05) or $Pde4b^{+/-}$ (*p<0.05) microglia, suggesting a compensatory upregulation to compensate for the loss of *Pde4b* in $Pde4b^{-/-}$ microglia (**Figure 4.B**). The gene expression of *Pde7b* was not different between the groups (**Figure 4.C**). *Pde8a* expression was significantly lower in $Pde4b^{+/-}$ microglia than $Pde4b^{-/-}$ microglia (*p<0.001) (**Figure 4.D**). These results indicate no compensation for $Pde4b^{+/-}$ microglia, while $Pde4b^{-/-}$ microglia potentially counteract the loss of *Pde4b* expression with upregulating *Pde7a*.

APP/PS1 mice with phagocyte-specific Pde4b expression showed impaired spatial and working memory at baseline – APP/PS1 mice were subjected to a BMT, receiving bone marrow from $Pde4b^{+/+}$, $Pde4b^{+/-}$, or $Pde4b^{-/-}$ mice to elucidate the effect of CNS phagocyte-specific *Pde4b* expression on cognitive decline in the context of AD. The OLT was used to assess spatial memory at baseline (6 months of age) (**Figure 5.A**). A time delay of 1 h revealed that only the WT and AD groups, receiving bone marrow from $Pde4b^{+/+}$ mice, were able to discriminate the moved object from the stationary object (*p<0.05) (**Figure 5.B**). In contrast, AD mice with microglial $Pde4b^{+/-}$ were not able to recognize the moved object, while AD-$Pde4b^{-/-}$ mice showed a trend to differentiate the moved object from the stationary object (**Figure 5.B**).
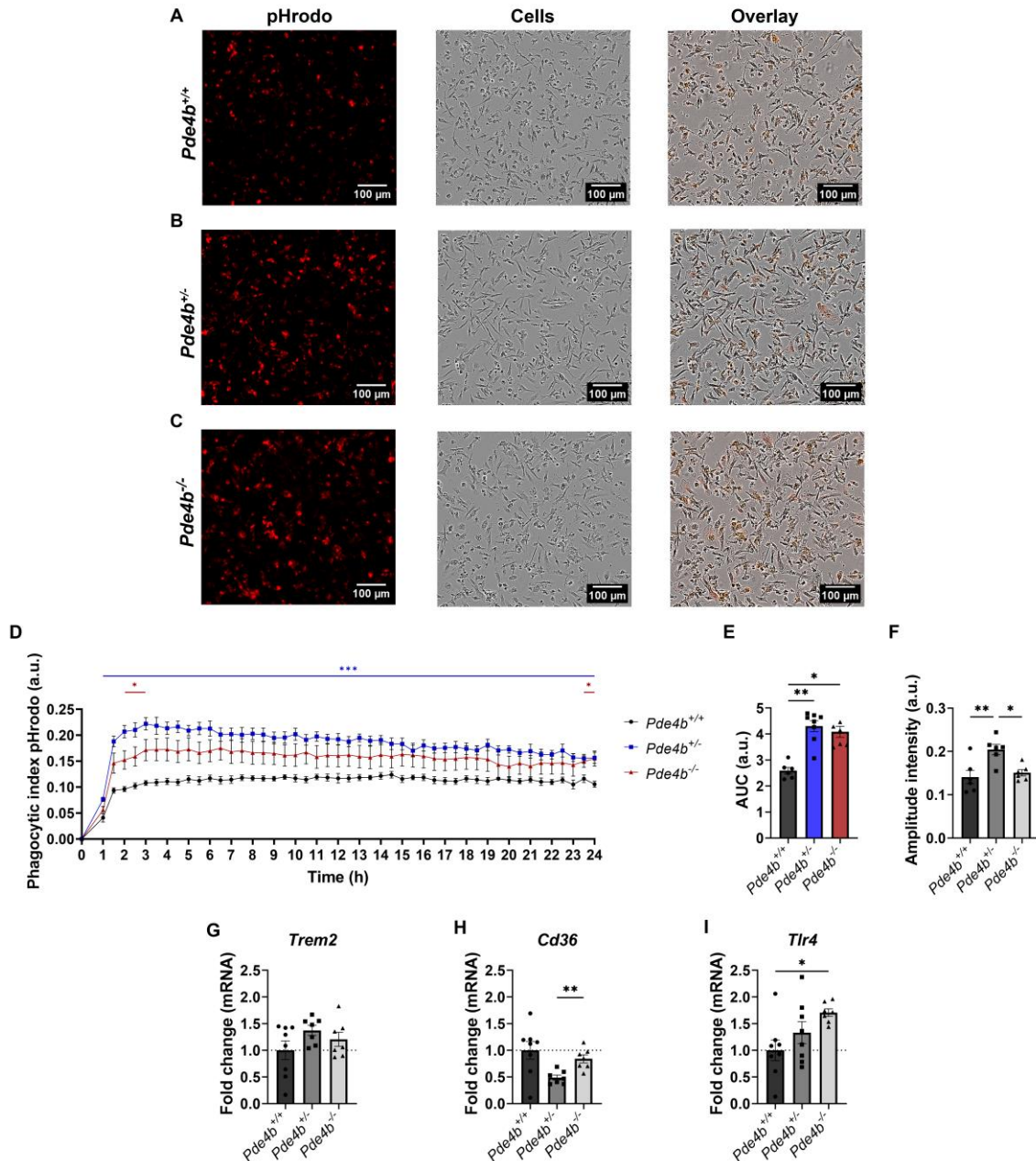
Figure 3: The microglial *Pde4b* phenotype shapes behavior and gene expression of phagocytosis-associated genes. Representative images of the pHrodo fluorescent signal, cells, and overlay pictures 3.5 h after synaptosome administration in (A) *Pde4b^{+/+}*, (B) *Pde4b^{+/-}*, or (C) *Pde4b^{-/-}* primary murine microglia. Scale bar 100 µm. (D) The phagocytic index of pHrodo was measured by live-cell imaging of pHrodo-labeled synaptosome uptake by murine microglia and calculated by dividing the area covered by pHrodo-positive cells by the total cell area of that image (n= 6-8 biological replicates). The blue line indicates differences between *Pde4b^{+/+}* and *Pde4b^{+/-}* microglia, while the red line indicates a difference between *Pde4b^{+/+}* and *Pde4b^{-/-}* microglia. (E) The area under the curve was determined for the (D) phagocytic index of pHrodo in *Pde4b^{+/+}*, *Pde4b^{+/-}*, or *Pde4b^{-/-}* microglia. (F) The amplitude of intensity was defined by the difference between the maximum intensity at 2-6 h and the minimum intensity normalized to the minimum intensity using Fiji. The mRNA expression of phagocytosis genes (G) *Trem2*, (H) *Cd36*, and (I) *Tlr4* are relative to the mRNA expression of respective genes in *Pde4b^{+/+}* microglia normalized to housekeeping genes *Cyca* and *Ywhaz* (n=6-8 biological replicates). Data are represented as mean ± SEM and analyzed with a (D) Mixed-effect analysis with Tukey's correction for multiple comparisons, (E) Kruskal-Wallis test with Dunn's correction for multiple comparisons, (F) one-way ANOVA with Tukey's correction for multiple comparisons, and (G-I) Welsh ANOVA test with Dunnett's correction for multiple comparisons. *p<0.05 and **p<0.01. AUC, Area under the curve; a.u., arbitrary unit.
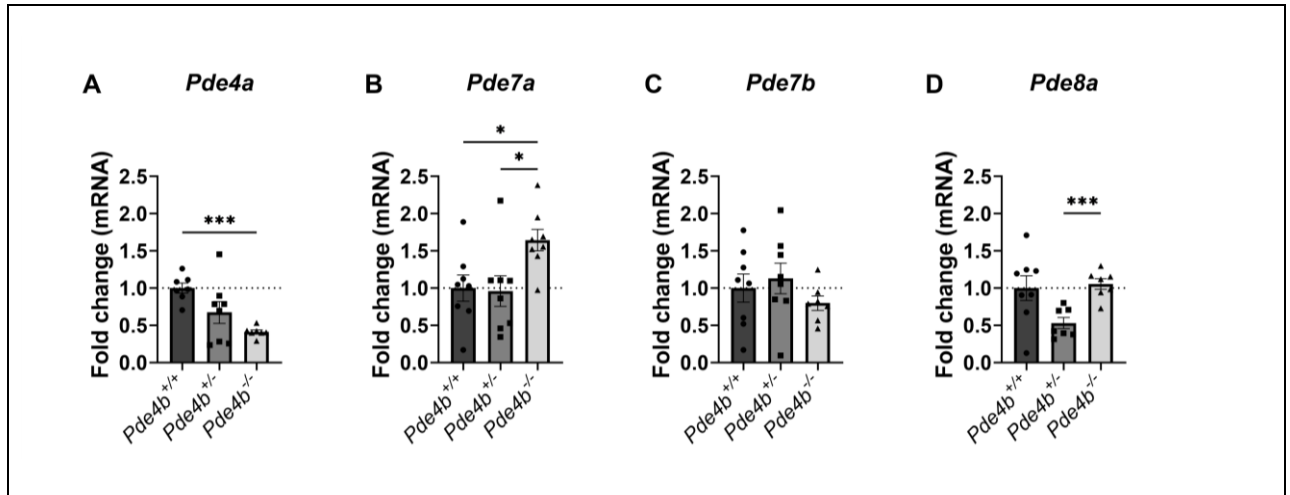
Figure 4: Changes in *Pde4b* expression in microglia lead to altered expression of cAMP-specific phosphodiesterase genes. (A-D) mRNA expression of cAMP-specific phosphodiesterase (A) *Pde4a*, (B) *Pde7a*, (C) *Pde7b*, and (D) *Pde8a* expressed relative to *Pde4b*$^{+/+}$ expression of respective genes with *Cyca* and *Ywhaz* as reference genes. Data are represented as mean ± SEM and analyzed with a Welsh ANOVA test with Dunnets's correction for multiple comparisons *p<0.05, ***p<0.001, n=6-8 biological replicates.
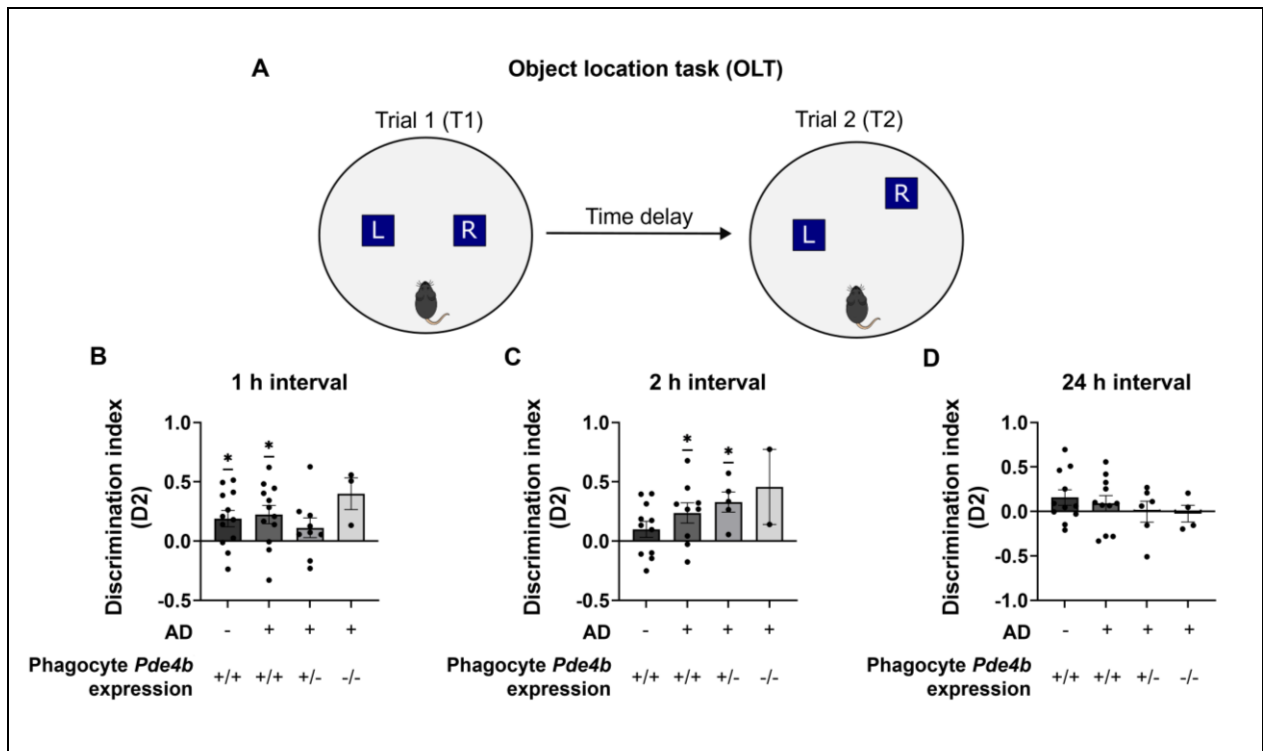

Figure 5: APP/PS1 mice with phagocyte-specific *Pde4b* expression in the CNS showed impaired spatial memory at baseline (6 months of age). (A) APP/PS1 mice with phagocyte-specific expression of *Pde4b* in the CNS were subjected to an OLT with a time delay of (B) 1, (C) 2, or (D) 24 h to assess spatial memory at baseline (age of 6 months). Spatial memory was calculated by D2, which represents the ratio of the time spent with the moved object compared to the stationary object in T2 whereby each trial lasted 4 min. Object movement in T2 was randomized with movement to either back or front as well as left-right movement, indicated with either L or R, respectively in the blue box, which represents the object. Data are represented as mean ± SEM of the D2 values with the black dots representing the mean of three individual mouse values and analyzed using a one-sample t-test to detect differences from 0, *p<0.05. Sample size OLT: $n_{WT-Pde4b+/+}$= 11-12, $n_{AD-Pde4b+/+}$= 9-12, $n_{AD-Pde4b+/-}$= 4-8, $n_{AD-Pde4b-/-}$=1-4. CNS, Central nervous system; OLT, Object Location Task; T1, Trial 1; T2, Trial 2; D2, Discrimination index; AD, Alzheimer's disease.
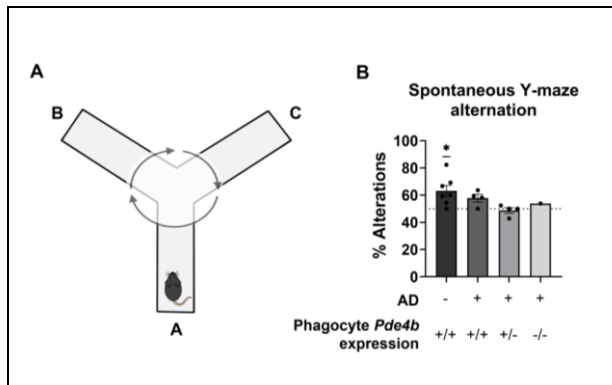
Figure 6: AD mice demonstrated impaired working memory at baseline (6 months of age). (A) APP/PS1 mice with phagocyte-specific *Pde4b* expression were placed in a Y-maze and spontaneous alternation was manually recorded for 6 min to assess working memory. (B) Working memory was considered intact with a significant difference of 50% alternation. Data are represented as mean ± SEM and analyzed with a one-sample t-test, *p<0.05, $n_{WT-Pde4b+/+}$= 7, $n_{AD-Pde4b+/+}$= 4, $n_{AD-Pde4b+/-}$= 4, $n_{AD-Pde4b-/-}$= 1. AD, Alzheimer's disease.

The 2 h delay in the OLT was demonstrated to be more difficult for WT-*Pde4b*$^{+/+}$ mice. However, AD-*Pde4b*$^{+/+}$ and AD-*Pde4b*$^{+/-}$ mice were able to recognize the displaced object (*p<0.05) (**Figure 5.C**). The inability to recognize the moved object in the OLT after 1 h and 2 h by different mice groups at baseline indicated impaired spatial memory of the used experimental mouse model (**Figure 5**). Lastly, no mice group could discern the moved object with a 24 h time delay OLT (**Figure 5.D**). The spontaneous Y-maze alternations test was used to examine working memory (7 months of age) (**Figure 6.A**). The spontaneous Y-maze alternation test revealed intact working memory in WT-*Pde4b*$^{+/+}$ mice (*p<0.05) while working memory was impaired in all AD groups (**Figure 6.B**).

AD chimeras demonstrated a genotype-dependent mortality – A bone marrow transplantation was used with WT or AD mice receiving bone marrow from *Pde4b*$^{+/+}$, *Pde4b*$^{+/-}$, or *Pde4b*$^{-/-}$ mice to investigate the phagocyte-specific effect of *Pde4b* expression in the CNS on cognitive function in AD. Unfortunately, an increased mortality over time was observed in the used chimeras. Early mortality was demonstrated shortly after the immuno-susceptible period (6 weeks post-BMT) in the AD-*Pde4b*$^{+/-}$ group and AD-*Pde4b*$^{-/-}$ group (**Figure 7.A**). The sudden death of five AD-*Pde4b*$^{-/-}$ mice on day 26 was observed,

while a more gradual decline in survival probability was perceived in the AD-*Pde4b*$^{+/-}$ group. The WT and AD group, which received bone marrow from *Pde4b*$^{+/+}$ mice, did not suffer from increased mortality before single housing (day 78) (**Figure 7.A**). After single housing, especially the AD-*Pde4b*$^{-/-}$ group demonstrated a rapid decrease in mortality compared to a more gradual decline in the other groups. Although the AD-*Pde4b*$^{+/+}$ mice did not show a significant decrease in mortality before the single housing, an increased mortality rate was observed starting from day 102 (**Figure 7.A**). The animals were sacrificed at day 136 and a significant (***p<0.001) *Pde4b* genotype-specific survival probability was observed between WT-*Pde4b*$^{+/+}$ and AD-*Pde4b*$^{-/-}$ mice (**Figure 7.A**). The mortality of the animals was preceded by heavy breathing, arched posture, and decreased locomotion. Additionally, a considerable fraction of mice lost over 5% of weight in the last 36 days before sacrifice (**Figure 7.B**).

Bone marrow transplanted animals have an altered heart function – During the sacrifice of the BMT animals, a considerable amount of pleural fluid was detected in the thorax. Research showed that an accumulation of pleural fluid was accompanied by increased mortality starting 25 weeks after radiation (47). Radiation-induced lung and cardiac injury are well known (47, 48). The BMT experiment was repeated, and an echocardiography was taken after the immune susceptible period (6 weeks post-radiation) to unravel the underlying cause of the unexpected deaths. It should be noted that there are differences between the WT and AD groups (**Table 2**). However, for the WT group, a female was used. In contrast, a male mouse was used in the AD group, which can explain the differences between these groups since it was shown that there are no differences between the WT animals and APP/PS1 mice for the measured parameters in this project (49). The cardiac parameters of a single mouse per group are represented in (**Table 2**). The ejection fraction (EF) of all mice were in the reference range of 55-70% except for the AD-*Pde4b*$^{+/+}$ group. However, the stroke volume (SV), cardiac output (CO), and fractional shortening (FS) were lower in all BMT groups apart from the AD-*Pde4b*$^{-/-}$ mouse, which only showed a reduced FS compared to the WT and AD mouse.
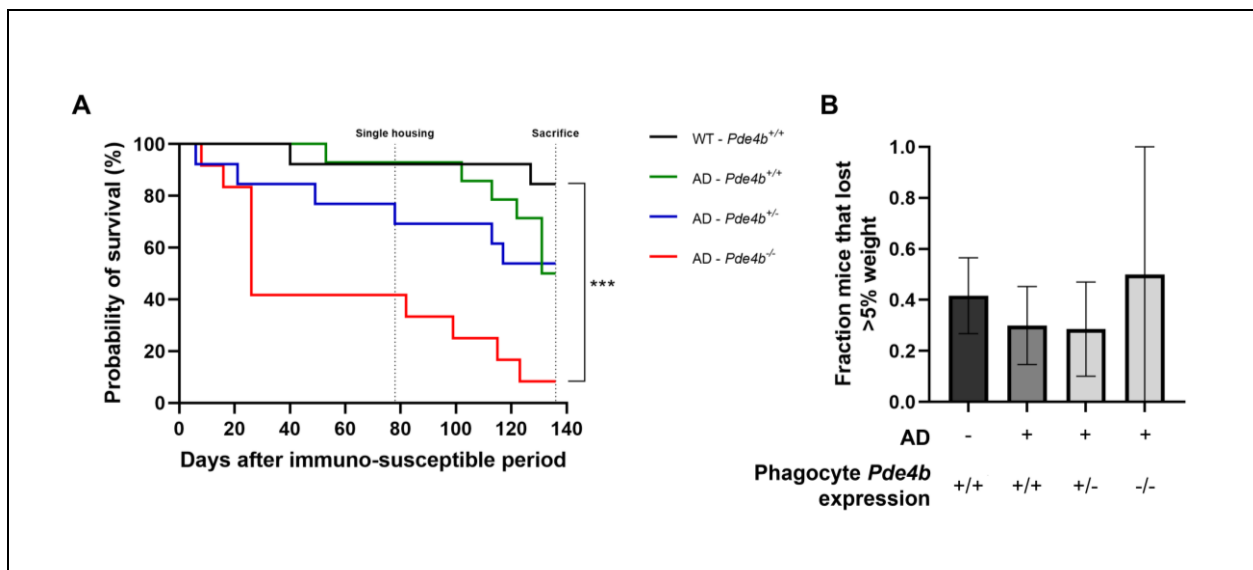
Figure 7: A *Pde4b* genotype-dependent survival is present in BMT chimeras. C57BL/6 WT or AD mice were irradiated with 8 Gy prior to receiving bone marrow from *Pde4b*$^{+/+}$, *Pde4b*$^{+/-}$, or *Pde4b*$^{-/-}$ donor C57BL/6 mice. (A) Kaplan-Meier curve of WT mice with *Pde4b*$^{+/+}$ expression, AD mice with *Pde4b*$^{+/+}$, *Pde4b*$^{+/-}$, or *Pde4b*$^{-/-}$ expression are represented with a black, green, blue, or red line, respectively. The animals were single-housed starting on day 78 for behavior assessment and sacrificed on day 136. The days of survival are depicted as the days after the immuno-susceptible period (6 weeks post BMT). (B) Fraction of mice that lost over 5% of body weight (g) at the day of death or sacrifice compared to the weight at day 100. Data are represented as mean ± SEM and analyzed with (A) Logrank analysis with Bonferroni correction for multiple comparisons (B) a Kruskal Wallis test with Dunn's correction for multiple comparisons, ***p<0.001. BMT, bone marrow transplantation; WT, Wild-type; AD, APP/PS1 mice.

The left ventricular anterior wall thickness (AWT) during systole (AWTs) and diastole (AWTd) showed variations between the different groups. The thickness of the left ventricular posterior wall (PWT) during systole (PWTs) and diastole (PWTd) was increased in WT-*Pde4b*$^{+/+}$, AD-*Pde4b*$^{+/+}$, and AD-*Pde4b*$^{-/-}$ mouse compared to the WT mouse but not to the AD mouse (**Table 2**). Additionally, in all groups that underwent a BMT, an abnormal heart cycle was observed characterized by unsynchronized closure of the heart valves (Data not shown). The visible and measured cardiac parameters give a first indication that the cardiac function in animals which received a BMT was adjusted.

DISCUSSION

Excessive synaptic elimination is correlated with the degree of cognitive decline in AD patients (50). Microglia are crucial mediators in regulating synaptic plasticity by strengthening existing synapses and eliminating redundant synapses (8). However, the dysregulation of microglial activity is suggested to contribute to excessive synaptic elimination in AD (22). PDE4 inhibition showed to cease cognitive decline and modulate microglia reactivity. Unfortunately, the clinical translation of PDE4 is hampered due to its severe emetic side effects (51). The PDE4 subtype PDE4B was demonstrated to be upregulated in microglia during AD and revealed to play a vital role in modulating the inflammatory reactions of microglia during CNS pathology (25, 41). The immune-modulating role of PDE4 inhibition on microglia is hypothesized to be attributed to PDE4B inhibition. Hence, PDE4B inhibition has the potential to orchestrate microglia function without causing the emetic side effects observed during general PDE4 inhibition. Therefore, we elucidated the effect of PDE4B on microglial morphology, synaptic phagocytosis, and cognitive function in a rodent model of AD. Microglia are characterized in the adult brain by a ramified phenotype recognized by a small cell body, extensive processes, and fine filopodia to execute its surveillance function. In contrast, microglia in AD are identified by a small appearance accompanied by a decrease in process number and overall motility (52). Microglia morphology strongly correlates with its function, and hence, we investigated the effect of PDE4, PDE4B, and PDE4D inhibition on primary

Table 2: Mice have altered cardiac function 6 weeks after a bone marrow transplantation preceded with 8 Gy radiation. Cardiac parameters are represented for animals that did not suffer from a bone marrow transplantation (WT and AD mouse) or did suffer from a bone marrow transplantation (WT-*Pde4b*$^{+/+}$, AD-*Pde4b*$^{+/+}$, or AD-*Pde4b*$^{-/-}$). The parameters represent the data of a single mouse whereby all groups were 3-month-old females beside the AD mouse was a 3-month-old male. The echocardiography was performed 6 weeks after the bone marrow transplantation.

	WT	AD	WT-*Pde4b*$^{+/+}$	AD-*Pde4b*$^{+/+}$	AD-*Pde4b*$^{-/-}$
EF (%)	66.234	55.77	70.32	29.086	68.602
SV (µl)	33.688	39.087	21.471	13.487	34.241
CO (ml/min)	17.215	23.491	11.722	6.012	17.959
FS (%)	14.567	7.070	5.670	4.250	4.020
AWTs (mm)	1.543	1.118	1.067	1.179	1.090
AWTd (mm)	0.977	0.776	0.847	0.948	0.634
PWTs (mm)	1.162	1.578	1.421	1.248	1.297
PWTd (mm)	0.891	1.259	1.081	0.943	0.905

WT, Wild-type; AD, APP/PS1 mouse; EF, Ejection fraction; SV, Stroke volume; CO, Cardiac output; FS, Fractional shortening of the left ventricle; AWT, anterior wall thickness left ventricle; PWT, Posterior wall thickness left ventricle; s, systole; d, diastole.

murine microglial morphology. cAMP is a potent regulator for microglia motility observed by the rapid process retraction and the formation of highly motile filopodia during cAMP elevation (24, 53, 54). Altering cAMP levels via PDE modulation showed to regulate microglia morphology and motility. Pan PDE inhibition with 10 µM IBMX increased microglia roundness, motility, filopodia length, and filopodia number in brain slices and *in vitro*. These effects were mainly attributed to the inhibition of PDE3 since the used IBMX concentration predominantly inhibited PDE3. Additionally, PDE3B inhibition with 10 µM cilostamide or 500 µM amrinone instigated a filopodia-rich microglial phenotype (24). Our data demonstrate that cAMP-mediated regulation of microglia morphology can also be achieved by PDE4 inhibition, illustrated by a gain in circularity after 45 min of incubation with PDE4 inhibitor roflumilast. Our findings are supported *in vivo* whereby daily intragastrical administration of 0.5-1 mg/kg roflumilast for 4 weeks, after being exposed to chronic unpredictable mild stress for 12 weeks, reduced process length, area, and branching points of hippocampal microglia (55). In addition, our data give a first indication that PDE4 and PDE4B inhibition can increase filopodia motility and the number. The increase in filopodia motility and number is considered beneficial to promote microglia function in neurodegenerative disorders. Furthermore, a trend to decrease microglial complexity by PDE4D inhibition was observed and is considered advantageous to hamper synaptic phagocytosis (8). However, the less ramified microglia shape is considered detrimental in AD due to the inflammatory nature of this microglial phenotype (56-59). Despite this, PDE4D inhibition is known to not influence the immune function of microglia, while PDE4 and PDE4B inhibition showed to reduce immune activation of microglia by lowering TNF-α and IL-1β production along with promoting (Arginase 1) Arg1 production (25, 39, 40). Although microglia morphology is correlated with immune function, the ability of PDE4D inhibition to lower microglial ramifications without influencing inflammatory status can be attributed to the spatiotemporal control of cAMP levels in cells by A-kinase-anchoring proteins (AKAP) (60). AKAP binds cAMP-regulated proteins in specific cellular domains leading to the subcellular control of cAMP. Therefore, AKAP complexes with PDE4D near microglial microtubules can be responsible for modulating process motility without influencing immune function. Indeed, PDE4D was found to be accumulated in microtubules within dendritic shafts of neurons of the dorsolateral prefrontal cortex of macaques (61). In addition, PDE4D appeared to regulate microtubule dynamics by

phosphorylating tau, leading to microtubule disassembly (62). Despite this, the subcellular location and interaction of PDE4D with the microglial cytoskeleton remains to be elucidated. PDE4D inhibition was not tested in relation to microglial surveillance and, thus, can not be excluded to regulate actin-dependent filopodia movement. Furthermore, a low sample size for filopodia motility experiments was available, and hence, replicating the surveillance experiments is needed to have a final conclusion of the role of different PDE4 subtypes in microglia motility. Lastly, PDE4 and PDE4B inhibition already showed to reduce TNF-α production by microglia, but the effect of the increased surveillant microglia phenotype with reduced processes on synaptic elimination is unknown. Consequently, the functional characterization of the observed microglia phenotype during PDE(B) inhibition on Aβ elimination and synaptic phagocytosis is demanded to unravel the consequences of PDE4(B) inhibition on microglial function in AD.

The dual functions of microglia in the CNS contribute to modulating CNS homeostasis but also the progression of neurodegenerative disorders. Microglia are the first line defense against harmful components, e.g., Aβ, and support neuronal communication by strengthening active synapses and eliminating weak synapses. In contrast, microglia mediate the chronic production of inflammatory mediators and excessive synaptic elimination in AD. The phagocytic behavior of microglia is key in executing its neuroprotective functions but also in the contribution of excessive synaptic elimination (63). Therefore, the influence of *Pde4b* on microglial phagocytosis was investigated. The phagocytic capacity of pHrodo-labeled synaptosomes by $Pde4b^{+/+}$, $Pde4b^{+/-}$, and $Pde4b^{-/-}$ murine microglia was used to elucidate the role of *Pde4b* on microglia-mediated synaptic elimination *in vitro*. Surprisingly, microglia with $Pde4b^{+/-}$ expression had more phagocytosing cells compared to $Pde4b^{+/+}$ microglia, while $Pde4b^{-/-}$ microglia only demonstrated an augmented number of phagocytosing cells than $Pde4b^{+/+}$ microglia during the peak time of phagocytosis. Moreover, $Pde4b^{+/-}$ microglia had increased phagocytic capacity compared to $Pde4b^{+/+}$ and $Pde4b^{-/-}$ microglia. The phagocytic capacity of heterozygous or knockout *Pde4b* expression in microglia is not investigated before. Research indicated that a physiological elevation

of cAMP promotes phagocytosis of myelin through protein kinase A (PKA)-induced activation of complement receptors. In contrast, non-physiological elevations of cAMP, such as during PDE4 inhibition with rolipram, reduced microglial phagocytosis of myelin via PKA and exchange protein directly activated by cAMP (EPAC) (64, 65). The modulation of PKA and EPAC on phagocytosis is suggested through different mechanisms. First, prominent activation of PKA lowers actin polymerization, which inhibits phagocytosis by reducing pseudopodia formation (66, 67). Secondly, direct interactions with molecules associated with phagocytosis, e.g., complement receptors, could alter receptor-mediated phagocytosis (64). PDE4B is the predominant PDE4 subtype expressed by microglia. Heterozygous or no expression of *Pde4b* should alter microglial cAMP levels. However, the heterozygous expression or complete absence of *Pde4b* can potentially be compensated by modified gene expression of other *Pde* genes. Indeed, a significant upregulation of *Pde7a* was observed in unstimulated $Pde4b^{-/-}$ murine microglia. *Pde7* expression is low under physiological conditions in microglia (68). Nevertheless, *Pde7* inhibition *in vivo* reduced microgliosis and pro-inflammatory cytokine production in an experimental autoimmune encephalomyelitis model and spinal cord injury in mice, respectively, which indicates that PDE7 can influence microglia activity (69, 70). As a consequence, it is hypothesized that a physiological elevation of cAMP is present in $Pde4b^{-/-}$ microglia due to the upregulation of *Pde7a*. $Pde4b^{+/-}$ did not show altered cAMP-specific *Pde* expression except for lower *Pde8a* expression. Other cAMP-specific or dual-specific *Pde* subtypes can be measured in the future to have a comprehensive knowledge of feedback mechanisms. Subsequently, a cAMP ELISA can be performed to identify cAMP levels in both *Pde4b* genotypes to asses compensation on a functional level.

A qPCR of phagocytosis genes was performed in $Pde4b^{+/+}$, $Pde4b^{+/-}$, and $Pde4b^{-/-}$ microglia to further elucidate the mechanism behind the altered phagocytic behavior between the different *Pde4b* microglia genotypes. *Pde4b* expression did not influence *Trem2* expression in murine microglia. *Trem2* deficiency is known to limit Aβ phagocytosis, halt microglia migration, and enhance neurite damage (71-73). In addition, TREM2 protein expression and activity were

decreased in aged microglia or microglia derived from induced pluripotent stem cells from AD patients, respectively (74, 75). The ability of *Trem2* to enhance microglia-mediated Aβ phagocytosis was implied due to the upregulation of *Cd36* (76). *Pde4b$^{+/-}$* microglia had significantly reduced *Cd36* expression. *Cd36* is involved in receptor-mediated phagocytosis of Aβ plaques whereby the loss of *Cd36* impairs microglia to phagocytose Aβ plaques (77). Hence, these results imply a reduced capacity of Aβ plaque phagocytosis. In contrast, another receptor for Aβ plaque phagocytosis, *Tlr4*, was significantly upregulated in *Pde4b$^{-/-}$* microglia and showed a trend toward an increased expression in *Pde4b$^{+/-}$* microglia (78). *Tlr4*-mediated Aβ phagocytosis by microglia is associated with increased pro-inflammatory mediators (19, 79). The conflicting downregulation of *Cd36* and increased *Tlr4* expression in *Pde4b$^{+/-}$* and *Pde4b$^{-/-}$* are also observed in microglia from AD patients. Here, AD patients, and aged microglia in general, have a higher expression of pattern recognition receptors, e.g., *Tlr4*, and lower *Cd36* expression in activated microglia (77, 80, 81). It was shown that repeated exposure to Aβ led to diminished *Tlr4* responses resulting in impaired Aβ clearance (82). Additionally, the upregulation of *Tlr4*, observed in AD patients, lowered *Cd36* expression, which contributed to reduced Aβ phagocytosis by microglia (83). This alternation in phagocytosis genes is considered to contribute to the dysfunctional phagocytic behavior of microglia in AD. Therefore, our results suggest that *Pde4b$^{+/-}$* microglia display a phenotype associated with disrupted phagocytosis regulation. However, the capacity to phagocytose Aβ was not evaluated in this project. Additionally, receptors involved in synaptic phagocytoses, such as complement receptor 3 (CR3), were not investigated, and the protein level of the different receptors were also not determined. Besides, these qPCR experiments were performed on unstimulated microglia, and thus, expression profiles of the different receptors can be altered during microglia activation. Lastly, PDE4 inhibition was demonstrated to reduce microglial phagocytosis (64, 65). Interestingly, especially PDE4B and PKA were colocalized with the phagosome in the initial stages of phagocytosis in monocytes, whereby cAMP-mediated phagocytosis inhibition with forskolin prevented the colocalization of HSPPDE4B and PKA to the site of the particles (84). Hence,

modulating cAMP levels with PDE4B inhibition is promising to induce another effect on microglia phagocytosis compared to differential *Pde4b* expression based on literature. Unfortunately, due to contaminations and the inappropriate working of the incuyte, and the breakdown of the incuyte, the effect of PDE4B inhibition could not be tested.

Preliminary data demonstrated improved spatial memory with an OLT after 5 h in APP/PS1 mice treated for 100 days starting at P20 with 3 mg/kg PDE4B inhibitor A33. To elucidate the microglia-specific contribution of modulating *Pde4b* on cognitive function in AD, a BMT with microglia depletion was used to induce phagocyte-specific expression of *Pde4b* in the CNS. The OLT was used to assess spatial memory at baseline (6 months of age) in AD chimeras. The OLT is based on the intrinsic curiosity of mice to explore new situations and objects. Therefore, displacement of an object is considered novel, leading to increased exploration time with the moved object (85). A 24 h trial was executed as a control since no mouse should be able to discriminate between the stationary and moved object, as could be observed in our experiment (85, 86). Nevertheless, a second control is a 1 h interval where mice should be able to recognize the moved object, but this was only observed in the WT and AD group receiving bone marrow from *Pde4b$^{+/+}$* mice, indicating already compromised spatial memory at baseline in the AD-*Pde4b$^{+/-}$* and AD-*Pde4b$^{-/-}$* group. Despite this, it was decided to continue with a 2 h delay to assess spatial memory. This 2 h delay demonstrated impaired spatial memory in the WT-*Pde4b$^{+/+}$* group, while the AD-*Pde4b$^{+/-}$* and AD-*Pde4b$^{-/-}$* groups could discriminate the moved object from the stationary object. The impaired capacity to discriminate the stationary from the moved object by multiple mouse groups at different intervals suggests impaired spatial memory. However, WT-*Pde4b$^{+/+}$* mice had intact working memory, while all AD BMT groups had compromised working memory, indicated by no difference in spontaneous alternation of 50%. The impairment in spatial memory compared to intact working memory can be attributed to different brain regions involved in spatial and working memory (87, 88). Spatial memory in mice is processed in the dorsal hippocampus, while working memory encompasses different brain regions, including the medial prefrontal cortex, thalamus, and

hippocampus (88, 89). Cognitive deficits are a known result of whole-body radiation. Localized radiation with 10 Gy to the hippocampus and cortex in 2 months old mice resulted in impaired spatial memory assed with the Barnes maze but not with the Morris water maze at 5 months of age (90). In contrast, other research demonstrated that irradiation with 5 Gy could already impair spatial memory tested by the Morris water maze but not the Barnes maze 3 months after radiation (91). Data suggested that the radiation-induced (5-10 Gy) deficits were attributed to the lower proliferation of neurons in the hippocampus (90, 91). Five Gy of radiation in mice induced a prominent increase in reactive microglia and infiltrated monocytes 1 and 3 months after radiation, suggesting that chronic inflammation is present after radiation (91). Therefore, the used radiation dose can potentially contribute to accelerating hippocampus-regulated spatial memory deficits. However, it should be noted that radiation affects microglia in a dose-dependent manner (92). Kim *et al.* reported that 24 h after 1 Gy radiation upon lipopolysaccharide (LPS) induction in microglia-like BV2 cells reduced the expression of pro-inflammatory cytokines (TNF-α and IL-1β) and stimulated the expression of anti-inflammatory cytokines (Tumor growth factor alpha and beta, IL-10). Additionally, daily radiation with 5 Gy in 5XFAD mice reduced amyloid plaque load and improved spatial memory assessed with the Moris water maze (93). The dose-dependent effect of radiation on amyloid beta pathology, inflammation, and cognition led to the development of multiple pilot studies investigating the therapeutic potential of low-dose radiation for the treatment of AD (94, 95).

The failed cognitive tests can also be explained by the deteriorated health of the mice. A profound dropout of AD-*Pde4b*$^{-/-}$ animals was observed, leaving only 1 animal of the initial 16 left for cognitive tests. To improve the health of the animals, it was decided to supply them with food and water in the form of a hydrogel in the cage. Nevertheless, the mortality was further increased during the period of cognitive testing. These mice exhibited an arched posture, weight loss, heavy breathing, impaired exploration, and decreased responsiveness leading to sacrifice when endpoints were reached, and hence, a smaller sample size with high variability was present in all cognitive tests. APP/PS1 mice are more prone to seizures, but the prominent death of our experimental groups is unlikely to be solely

attributed to seizures (96). The progressive deterioration in health led to the decision to sacrifice all animals. During this sacrifice, a profound amount of lung fluid was detected in the thorax. Jackson *et al.* demonstrated that a single dose of 12.5 and 15 Gy radiation led to a progressively increased breathing rate starting 4 months after the radiation coincident with ameliorated mortality. Additionally, lower lung volumes were observed, attributed to pleural fluid-induced atelectasis. Pleural fluid was detected 26 weeks after irradiation, which is in coherence with the observed pleural fluid at sacrifice (24.5 weeks) in this project (47). Further research supported radiation-induced pneumonitis in the lungs accompanied by increased mortality (97). An accomplished mechanism of lung pathology upon radiation-induced lung disease is the reduced capacity of resident alveolar macrophages to proliferate. As a consequence, bone marrow-derived macrophages enter the lungs to compensate for the impaired proliferation of resident macrophages (98). These infiltrated macrophages secrete inflammatory products, such as nitric oxide synthase (NOS) and interferon-gamma (INF-γ), and contribute to chronic inflammation via the formation of foamy macrophages (99, 100). Profound lung remodeling is hypothesized to induce hypoperfusion and, eventually, pleural effusion. Besides radiation-induced lung disease, C57BL/6 mice are susceptible to radiation-induced cardiac remodeling (48, 101). Myocardial cells are more resilient to radiation-induced damage due to their low mitogenic capacity. However, endothelial cells, supplying the heart, are known to release inflammatory mediators shortly after radiation (48, 102). Additionally, radiated arteries had more macrophages colocalized with nuclear factor kappa B (NF-κB), leading to the increased attraction of other immune cells and enhanced inflammation (103). The environment with oxidative stress and inflammatory cytokines stimulate fibroblast pathways leading to cardiac fibrosis and, eventually, reduced cardiac motility (101). Additionally, a single dose of 15 Gy radiation reduced the EF and FS of C57BL/6 mice 12 months after radiation (104). In a new BMT experiment, a single echocardiography of one mouse per group, 6 weeks after 8 Gy radiation, demonstrated already altered cardiac parameters. APP/PS1 mice are known to have altered excitation-coupling, but not in proportions leading to differences in cardiac parameters (49). Our results suggest hampered left ventricular

contractility in radiated animals, observed by a reduced FS in all BMT groups. Additionally, the reduction in SV in WT and AD groups receiving bone marrow from $Pde4b^{+/+}$ animals indicated problems with diastolic function or decreased contractility of the left ventricle. The decrease in SV can be attributed to impaired relaxation (diastole) leading to reduced CO (105). As a compensation mechanism, cardiac hypertrophy can be stimulated to preserve the EF (105). Indeed, increased PWT during systole and diastole was observed. Therefore, it is postulated that the radiation induced heart failure with preserved ejection fraction (106). The observed cardiac phenotype is characterized by dyspnea and congestion in patients and rodent models (107). Due to the observation of ameliorated breathing frequency and pleural fluid, this cardiac phenotype could also be a contributor to the observed early mortality after radiation. However, it should be noted that the EF of AD-$Pde4b^{+/+}$ animals was not preserved and severely decreased, potentially because of a more advanced stage of heart remodeling. In addition, the heart of only a single mouse per group was visualized to get a first indication of cardiac function. Besides the measured parameters, a dysfunctional heart cycle was observed (Data not shown) with arrhythmic contraction and not synchronized valve closure and opening. However, additional echocardiography's of multiple animals per group are planned to support this observation. Subsequently, cardiac remodeling can be detected with a picrosirius red staining, and infiltrated immune cells can be stained. Besides cardiac evaluation, congestion and lung function can be determined post-mortem by measuring the difference in wet and dry weight and pleural fluid volume.

Macrophages are suggested, amongst others, as key players in radiation-induced lung and cardiac injury. In both the lungs and the heart, a senescent phagocyte phenotype is observed after radiation. Radiated murine-derived bone marrow macrophages with 4-10 Gy display senescent markers such as β-galactosidase, p16, and p21 accompanied by elevated pro-fibrogenic factors such as Arg-1 implied to stimulate lung fibrosis (99). Furthermore, radiated macrophages *in vitro* have impaired efferocytosis of apoptotic cells leading to the accumulation of cellular debris (108). The senescent macrophage phenotype was associated with increased reactive oxygen species expression and *Tnf-α* (108). Interestingly, *Cd36* was shown to be upregulated

and crucial to mediate macrophage phagocytosis of dead lung cells leading to inflammatory foamy macrophage formation (109). In addition, *Tlr4* signaling is suggested to amplify inflammatory reactions through the activation of reactive oxygen species and hence, contributing to sustained inflammation in the radiated lung and heart (109-111). Both *Cd36* and *Tlr4* were demonstrated to have altered baseline expression in $Pde4b^{+/-}$ and $Pde4b^{-/-}$ murine microglia. Although these are only 2 genes of the many genes and products involved in the radiated injury, differential *Pde4b* expression shows to influence receptors associated with phagocytosis in AD and radiation-induced injury. Additionally, others show that *Pde4b* knockout influences inflammatory responses in phagocytes, e.g., the fibrotic stimulating cytokine IL-6 is upregulated upon spinal cord injury in *Pde4b* knockout animals (39, 40, 112). The crucial role of bone marrow-derived macrophages in radiation-induced injury, the altered phagocytic behavior in *Pde4b* depleted microglia, along with differential expression of effector genes for phagocytosis, e.g., *Cd36* and *Tlr4*, and inflammatory genes can give an explanation for *Pde4*-genotype dependent mortality rates in the used animal model. In the future, the effect of microglia-specific *Pde4b* expression can be elucidated using a total marrow radiation (TMR) instead of total body radiation (TBR). With TMR, computed tomography-guided anatomical positioning of radiation is used to only radiate the bone marrow, and this showed to reduce organ damage without limiting donor engraftment (113). Another possibility is to generate a Cre/Lox system to induce phagocyte-specific expression of *Pde4b* in microglia during the period that synaptic elimination arises in APP/PS1 mice (114). Lastly, post mortem investigation of the number of synapses, microgliosis, and Aβ accumulation can give a further indication about the microglia specific effect of *Pde4b* on cognitive function in AD.

CONCLUSION

In conclusion, subtype-specific inhibition of PDE4 subtypes was demonstrated to influence microglia morphology and motility. PDE4D inhibition showed a trend to decrease microglia complexity, while PDE4B inhibition gave a first indication to promote filopodia formation and motility. Both the decrease in processes and improved motility can be beneficial to cease synaptic elimination in AD. In contrast to our hypothesis, heterozygous or homozygous

deficiency of microglial *Pde4b* increased pHrodo-labeled synaptosome phagocytosis accompanied by altered expression of phagocytosis genes *Cd36* and *Tlr4*. However, an upregulation of other cAMP-specific *Pdes* was observed in *Pde4b$^{-/-}$* microglia indicating that *Pde4b* inhibition can have a differential effect on microglial phagocytosis. The microglia-specific effect of *Pde4b* expression remains to be unclear due to the unexpected death of AD bone marrow chimeras due to postulated radiation-induced lung and cardiac injury. In the future, the functional consequences of altered *Pde4b* expression in microglia on cAMP levels is demanded to elucidate if feedback mechanisms are present. Subsequently, the effect of PDE4B inhibition on microglial phagocytosis is needed to unravel the effect of PDE4B on microglia. Finally, other mouse models, such as TMR or Cre/Lox systems, can be used to elucidate the contribution of *Pde4b* on microglia-mediated synaptic elimination and cognitive function in AD

REFERENCES
1.   Breijyeh Z, Karaman R. Comprehensive Review on Alzheimer's Disease: Causes and Treatment. Molecules. 2020;25(24).
2.   WHO. Dementia. 2017.
3.   Knopman DS, Amieva H, Petersen RC, Chetelat G, Holtzman DM, Hyman BT, et al. Alzheimer disease. Nat Rev Dis Primers. 2021;7(1):33.
4.   Vaz M, Silvestre S. Alzheimer's disease: Recent treatment strategies. Eur J Pharmacol. 2020;887:173554.
5.   Terry RD, Masliah E, Salmon DP, Butters N, DeTeresa R, Hill R, et al. Physical basis of cognitive alterations in Alzheimer's disease: synapse loss is the major correlate of cognitive impairment. Ann Neurol. 1991;30(4):572-80.
6.   Mecca AP, O'Dell RS, Sharp ES, Banks ER, Bartlett HH, Zhao W, et al. Synaptic density and cognitive performance in Alzheimer's disease: A PET imaging study with [(11) C]UCB-J. Alzheimers Dement. 2022;18(12):2527-36.
7.   Yu W, Lu B. Synapses and dendritic spines as pathogenic targets in Alzheimer's disease. Neural Plast. 2012;2012:247150.
8.   Rombaut B, Kessels S, Schepers M, Tiane A, Paes D, Solomina Y, et al. PDE inhibition in distinct cell types to reclaim the balance of synaptic plasticity. Theranostics. 2021;11(5):2080-97.
9.   Kettenmann H, Kirchhoff F, Verkhratsky A. Microglia: new roles for the synaptic stripper. Neuron. 2013;77(1):10-8.
10.   Smolders SM, Kessels S, Vangansewinkel T, Rigo JM, Legendre P, Brone B. Microglia: Brain cells on the move. Prog Neurobiol. 2019;178:101612.
11.   Lim SH, Park E, You B, Jung Y, Park AR, Park SG, et al. Neuronal synapse formation induced by microglia and interleukin 10. PLoS One. 2013;8(11):e81218.
12.   Harry GJ. Microglia during development and aging. Pharmacol Ther. 2013;139(3):313-26.
13.   Miyanishi K, Sato A, Kihara N, Utsunomiya R, Tanaka J. Synaptic elimination by microglia and disturbed higher brain functions. Neurochem Int. 2021;142:104901.
14.   Presumey J, Bialas AR, Carroll MC. Complement System in Neural Synapse Elimination in Development and Disease. Adv Immunol. 2017;135:53-79.
15.   Qin Q, Wang M, Yin Y, Tang Y. The Specific Mechanism of TREM2 Regulation of Synaptic Clearance in Alzheimer's Disease. Front Immunol. 2022;13:845897.
16.   Wolf SA, Boddeke HW, Kettenmann H. Microglia in Physiology and Disease. Annu Rev Physiol. 2017;79:619-43.
17.   Miyamoto A, Wake H, Ishikawa AW, Eto K, Shibata K, Murakoshi H, et al. Microglia contact induces synapse formation in developing somatosensory cortex. Nat Commun. 2016;7:12540.
18.   Wake H, Moorhouse AJ, Jinno S, Kohsaka S, Nabekura J. Resting microglia directly monitor the functional state of synapses in vivo and determine the fate of ischemic terminals. J Neurosci. 2009;29(13):3974-80.
19.   Fu R, Shen Q, Xu P, Luo JJ, Tang Y. Phagocytosis of microglia in the central nervous system diseases. Mol Neurobiol. 2014;49(3):1422-34.
20.   Basilico B, Ferrucci L, Ratano P, Golia MT, Grimaldi A, Rosito M, et al. Microglia control glutamatergic synapses in the adult mouse hippocampus. Glia. 2022;70(1):173-95.
21.   Ji K, Akgul G, Wollmuth LP, Tsirka SE. Microglia actively regulate the number of functional synapses. PLoS One. 2013;8(2):e56293.
22.   Rajendran L, Paolicelli RC. Microglia-Mediated Synapse Loss in Alzheimer's Disease. J Neurosci. 2018;38(12):2911-9.

23.   Hansen DV, Hanson JE, Sheng M. Microglia in Alzheimer's disease. J Cell Biol. 2018;217(2):459-72.

24.   Bernier LP, Bohlen CJ, York EM, Choi HB, Kamyabi A, Dissing-Olesen L, et al. Nanoscale Surveillance of the Brain by Microglia via cAMP-Regulated Filopodia. Cell Rep. 2019;27(10):2895-908 e4.

25.   Pearse DD, Hughes ZA. PDE4B as a microglia target to reduce neuroinflammation. Glia. 2016;64(10):1698-709.

26.   Ghosh M, Xu Y, Pearse DD. Cyclic AMP is a key regulator of M1 to M2a phenotypic conversion of microglia in the presence of Th2 cytokines. J Neuroinflammation. 2016;13:9.

27.   Hansen RT, 3rd, Zhang HT. Senescent-induced dysregulation of cAMP/CREB signaling and correlations with cognitive decline. Brain Res. 2013;1516:93-109.

28.   Luo Y, Kuang S, Li H, Ran D, Yang J. cAMP/PKA-CREB-BDNF signaling pathway in hippocampus mediates cyclooxygenase 2-induced learning/memory deficits of rats subjected to chronic unpredictable mild stress. Oncotarget. 2017;8(22):35558-72.

29.   Azevedo MF, Faucz FR, Bimpaki E, Horvath A, Levy I, de Alexandre RB, et al. Clinical and molecular genetics of the phosphodiesterases (PDEs). Endocr Rev. 2014;35(2):195-233.

30.   Ghosh M, Garcia-Castillo D, Aguirre V, Golshani R, Atkins CM, Bramlett HM, et al. Proinflammatory cytokine regulation of cyclic AMP-phosphodiesterase 4 signaling in microglia in vitro and following CNS injury. Glia. 2012;60(12):1839-59.

31.   Song GJ, Suk K. Pharmacological Modulation of Functional Phenotypes of Microglia in Neurodegenerative Diseases. Front Aging Neurosci. 2017;9:139.

32.   Heckman PR, Wouters C, Prickaerts J. Phosphodiesterase inhibitors as a target for cognition enhancement in aging and Alzheimer's disease: a translational overview. Curr Pharm Des. 2015;21(3):317-31.

33.   Guo H, Cheng Y, Wang C, Wu J, Zou Z, Niu B, et al. FFPM, a PDE4 inhibitor, reverses learning and memory deficits in APP/PS1 transgenic mice via cAMP/PKA/CREB signaling and anti-inflammatory effects. Neuropharmacology. 2017;116:260-9.

34.   Cheng YF, Wang C, Lin HB, Li YF, Huang Y, Xu JP, et al. Inhibition of phosphodiesterase-4 reverses memory deficits produced by Abeta25-35 or Abeta1-40 peptide in rats. Psychopharmacology (Berl). 2010;212(2):181-91.

35.   Wang H, Zhang FF, Xu Y, Fu HR, Wang XD, Wang L, et al. The Phosphodiesterase-4 Inhibitor Roflumilast, a Potential Treatment for the Comorbidity of Memory Loss and Depression in Alzheimer's Disease: A Preclinical Study in APP/PS1 Transgenic Mice. Int J Neuropsychopharmacol. 2020;23(10):700-11.

36.   Li H, Zuo J, Tang W. Phosphodiesterase-4 Inhibitors for the Treatment of Inflammatory Diseases. Front Pharmacol. 2018;9:1048.

37.   Schepers M, Paes D, Tiane A, Rombaut B, Piccart E, van Veggel L, et al. Selective PDE4 subtype inhibition provides new opportunities to intervene in neuroinflammatory versus myelin damaging hallmarks of multiple sclerosis. Brain Behav Immun. 2023;109:1-22.

38.   Paes D, Schepers M, Rombaut B, van den Hove D, Vanmierlo T, Prickaerts J. The Molecular Biology of Phosphodiesterase 4 Enzymes as Pharmacological Targets: An Interplay of Isoforms, Conformational States, and Inhibitors. Pharmacol Rev. 2021;73(3):1016-49.

39.   Wilson NM, Gurney ME, Dietrich WD, Atkins CM. Therapeutic benefits of phosphodiesterase 4B inhibition after traumatic brain injury. PLoS One. 2017;12(5):e0178013.

40.   Myers SA, Gobejishvili L, Saraswat Ohri S, Garrett Wilson C, Andres KR, Riegler AS, et al. Following spinal cord injury, PDE4B drives an acute, local inflammatory response and a chronic, systemic response exacerbated by gut dysbiosis and endotoxemia. Neurobiol Dis. 2019;124:353-63.

41.   Sebastiani G, Morissette C, Lagace C, Boule M, Ouellette MJ, McLaughlin RW, et al. The cAMP-specific phosphodiesterase 4B mediates Abeta-induced microglial activation. Neurobiol Aging. 2006;27(5):691-701.

42.   Leyh J, Paeschke S, Mages B, Michalski D, Nowicki M, Bechmann I, et al. Classification of Microglial Morphological Phenotypes Using Machine Learning. Front Cell Neurosci. 2021;15:701673.

43.   Bohlen CJ, Bennett FC, Bennett ML. Isolation and Culture of Microglia. Curr Protoc Immunol. 2019;125(1):e70.

44.   Vanmierlo T, Rutten K, Dederen J, Bloks VW, van Vark-van der Zee LC, Kuipers F, et al. Liver X receptor activation restores memory in aged AD mice without reducing amyloid. Neurobiol Aging. 2011;32(7):1262-72.

45.   Spittau B. Aging Microglia-Phenotypes, Functions and Implications for Age-Related

Neurodegenerative Diseases. Front Aging Neurosci. 2017;9:194.

46. Rosa JM, Farre-Alins V, Ortega MC, Navarrete M, Lopez-Rodriguez AB, Palomino-Antolin A, et al. TLR4 pathway impairs synaptic number and cerebrovascular functions through astrocyte activation following traumatic brain injury. Br J Pharmacol. 2021;178(17):3395-413.

47. Jackson IL, Vujaskovic Z, Down JD. Revisiting strain-related differences in radiation sensitivity of the mouse lung: recognizing and avoiding the confounding effects of pleural effusions. Radiat Res. 2010;173(1):10-20.

48. Hamada N, Kawano KI, Nomura T, Furukawa K, Yusoff FM, Maruhashi T, et al. Vascular Damage in the Aorta of Wild-Type Mice Exposed to Ionizing Radiation: Sparing and Enhancing Effects of Dose Protraction. Cancers (Basel). 2021;13(21).

49. Wang S, Wang L, Qin X, Turdi S, Sun D, Culver B, et al. ALDH2 contributes to melatonin-induced protection against APP/PS1 mutation-prompted cardiac anomalies through cGAS-STING-TBK1-mediated regulation of mitophagy. Signal Transduct Target Ther. 2020;5(1):119.

50. Cardozo PL, de Lima IBQ, Maciel EMA, Silva NC, Dobransky T, Ribeiro FM. Synaptic Elimination in Neurological Disorders. Curr Neuropharmacol. 2019;17(11):1071-95.

51. Richter W, Menniti FS, Zhang HT, Conti M. PDE4 as a target for cognition enhancement. Expert Opin Ther Targets. 2013;17(9):1011-27.

52. Damani MR, Zhao L, Fontainhas AM, Amaral J, Fariss RN, Wong WT. Age-related alterations in the dynamic behavior of microglia. Aging Cell. 2011;10(2):263-76.

53. Gyoneva S, Traynelis SF. Norepinephrine modulates the motility of resting and activated microglia via different adrenergic receptors. J Biol Chem. 2013;288(21):15291-302.

54. Gyoneva S, Shapiro L, Lazo C, Garnier-Amblard E, Smith Y, Miller GW, et al. Adenosine A2A receptor antagonism reverses inflammation-induced impairment of microglial process extension in a model of Parkinson's disease. Neurobiol Dis. 2014;67:191-202.

55. Xie J, Bi B, Qin Y, Dong W, Zhong J, Li M, et al. Inhibition of phosphodiesterase-4 suppresses HMGB1/RAGE signaling pathway and NLRP3 inflammasome activation in mice exposed to chronic unpredictable mild stress. Brain Behav Immun. 2021;92:67-77.

56. Vidal-Itriago A, Radford RAW, Aramideh JA, Maurel C, Scherer NM, Don EK, et al. Microglia morphophysiological diversity and its implications for the CNS. Front Immunol. 2022;13:997786.

57. Franco-Bocanegra DK, Gourari Y, McAuley C, Chatelet DS, Johnston DA, Nicoll JAR, et al. Microglial morphology in Alzheimer's disease and after Abeta immunotherapy. Sci Rep. 2021;11(1):15955.

58. Edler MK, Sherwood CC, Meindl RS, Munger EL, Hopkins WD, Ely JJ, et al. Microglia changes associated to Alzheimer's disease pathology in aged chimpanzees. J Comp Neurol. 2018;526(18):2921-36.

59. Franklin TC, Wohleb ES, Zhang Y, Fogaca M, Hare B, Duman RS. Persistent Increase in Microglial RAGE Contributes to Chronic Stress-Induced Priming of Depressive-like Behavior. Biol Psychiatry. 2018;83(1):50-60.

60. Kritzer MD, Li J, Dodge-Kafka K, Kapiloff MS. AKAPs: the architectural underpinnings of local cAMP signaling. J Mol Cell Cardiol. 2012;52(2):351-8.

61. Datta D, Enwright JF, Arion D, Paspalas CD, Morozov YM, Lewis DA, et al. Mapping Phosphodiesterase 4D (PDE4D) in Macaque Dorsolateral Prefrontal Cortex: Postsynaptic Compartmentalization in Layer III Pyramidal Cell Circuits. Front Neuroanat. 2020;14:578483.

62. Leslie SN, Datta D, Christensen KR, van Dyck CH, Arnsten AFT, Nairn AC. Phosphodiesterase PDE4D Is Decreased in Frontal Cortex of Aged Rats and Positively Correlated With Working Memory Performance and Inversely Correlated With PKA Phosphorylation of Tau. Front Aging Neurosci. 2020;12:576723.

63. Xie Z, Meng J, Wu Z, Nakanishi H, Hayashi Y, Kong W, et al. The Dual Nature of Microglia in Alzheimer's Disease: A Microglia-Neuron Crosstalk Perspective. Neuroscientist. 2022:10738584211070273.

64. Makranz C, Cohen G, Reichert F, Kodama T, Rotshenker S. cAMP cascade (PKA, Epac, adenylyl cyclase, Gi, and phosphodiesterases) regulates myelin phagocytosis mediated by complement receptor-3 and scavenger receptor-AI/II in microglia and macrophages. Glia. 2006;53(4):441-8.

65. Schmidt C, Schneble N, Muller JP, Bauer R, Perino A, Marone R, et al. Phosphoinositide 3-kinase gamma mediates microglial phagocytosis via lipid kinase-independent control of cAMP. Neuroscience. 2013;233:44-53.

66. Howe AK. Regulation of actin-based cell migration by cAMP/PKA. Biochim Biophys Acta. 2004;1692(2-3):159-74.

67. Ydrenius L, Majeed M, Rasmusson BJ, Stendahl O, Sarndahl E. Activation of cAMP-dependent protein kinase is necessary for actin rearrangements in human neutrophils during phagocytosis. J Leukoc Biol. 2000;67(4):520-8.

68. Bennett ML, Bennett FC, Liddelow SA, Ajami B, Zamanian JL, Fernhoff NB, et al. New tools for studying microglia in the mouse and human CNS. Proc Natl Acad Sci U S A. 2016;113(12):E1738-46.

69. Benitez-Fernandez R, Gil C, Guaza C, Mestre L, Martinez A. The Dual PDE7-GSK3beta Inhibitor, VP3.15, as Neuroprotective Disease-Modifying Treatment in a Model of Primary Progressive Multiple Sclerosis. Int J Mol Sci. 2022;23(22).

70. Paterniti I, Mazzon E, Gil C, Impellizzeri D, Palomo V, Redondo M, et al. PDE 7 inhibitors: new potential drugs for the therapy of spinal cord injury. PLoS One. 2011;6(1):e15937.

71. Wang Y, Ulland TK, Ulrich JD, Song W, Tzaferis JA, Hole JT, et al. TREM2-mediated early microglial response limits diffusion and toxicity of amyloid plaques. J Exp Med. 2016;213(5):667-75.

72. Mazaheri F, Snaidero N, Kleinberger G, Madore C, Daria A, Werner G, et al. TREM2 deficiency impairs chemotaxis and microglial responses to neuronal injury. EMBO Rep. 2017;18(7):1186-98.

73. Stoiljkovic M, Gutierrez KO, Kelley C, Horvath TL, Hajos M. TREM2 Deficiency Disrupts Network Oscillations Leading to Epileptic Activity and Aggravates Amyloid-beta-Related Hippocampal Pathophysiology in Mice. J Alzheimers Dis. 2022;88(3):837-47.

74. Thomas AL, Lehn MA, Janssen EM, Hildeman DA, Chougnet CA. Naturally-aged microglia exhibit phagocytic dysfunction accompanied by gene expression changes reflective of underlying neurologic disease. Sci Rep. 2022;12(1):19471.

75. Okuzono Y, Sakuma H, Miyakawa S, Ifuku M, Lee J, Das D, et al. Reduced TREM2 activation in microglia of patients with Alzheimer's disease. FEBS Open Bio. 2021;11(11):3063-80.

76. Kim SM, Mun BR, Lee SJ, Joh Y, Lee HY, Ji KY, et al. TREM2 promotes Abeta phagocytosis by upregulating C/EBPalpha-dependent CD36 expression in microglia. Sci Rep. 2017;7(1):11118.

77. Floden AM, Combs CK. Microglia demonstrate age-dependent interaction with amyloid-beta fibrils. J Alzheimers Dis. 2011;25(2):279-93.

78. Liu Y, Dai Y, Li Q, Chen C, Chen H, Song Y, et al. Beta-amyloid activates NLRP3 inflammasome via TLR4 in mouse microglia. Neurosci Lett. 2020;736:135279.

79. Calvo-Rodriguez M, Garcia-Rodriguez C, Villalobos C, Nunez L. Role of Toll Like Receptor 4 in Alzheimer's Disease. Front Immunol. 2020;11:1588.

80. Liu Y, Walter S, Stagi M, Cherny D, Letiembre M, Schulz-Schaeffer W, et al. LPS receptor (CD14): a receptor for phagocytosis of Alzheimer's amyloid peptide. Brain. 2005;128(Pt 8):1778-89.

81. Letiembre M, Hao W, Liu Y, Walter S, Mihaljevic I, Rivest S, et al. Innate immune receptor expression in normal brain aging. Neuroscience. 2007;146(1):248-54.

82. Go M, Kou J, Lim JE, Yang J, Fukuchi KI. Microglial response to LPS increases in wild-type mice during aging but diminishes in an Alzheimer's mouse model: Implication of TLR4 signaling in disease progression. Biochem Biophys Res Commun. 2016;479(2):331-7.

83. Li X, Melief E, Postupna N, Montine KS, Keene CD, Montine TJ. Prostaglandin E2 receptor subtype 2 regulation of scavenger receptor CD36 modulates microglial Abeta42 phagocytosis. Am J Pathol. 2015;185(1):230-9.

84. Pryzwansky KB, Kidao S, Merricks EP. Compartmentalization of PDE-4 and cAMP-dependent protein kinase in neutrophils and macrophages during phagocytosis. Cell Biochem Biophys. 1998;28(2-3):251-75.

85. Denninger JK, Smith BM, Kirby ED. Novel Object Recognition and Object Location Behavioral Testing in Mice on a Budget. J Vis Exp. 2018(141).

86. Vanmierlo T, Creemers P, Akkerman S, van Duinen M, Sambeth A, De Vry J, et al. The PDE4 inhibitor roflumilast improves memory in rodents at non-emetic doses. Behav Brain Res. 2016;303:26-33.

87. Tanimizu T, Kenney JW, Okano E, Kadoma K, Frankland PW, Kida S. Functional Connectivity of Multiple Brain Regions Required for the Consolidation of Social Recognition Memory. J Neurosci. 2017;37(15):4103-16.

88. Dexter TD, Palmer D, Hashad AM, Saksida LM, Bussey TJ. Decision Making in Mice During an Optimized Touchscreen Spatial Working Memory Task Sensitive to Medial

Prefrontal Cortex Inactivation and NMDA Receptor Hypofunction. Front Neurosci. 2022;16:905736.

89. Chockanathan U, Warner EJ, Turpin L, O'Banion MK, Padmanabhan K. Altered dorsal CA1 neuronal population coding in the APP/PS1 mouse model of Alzheimer's disease. Sci Rep. 2020;10(1):1077.

90. Raber J, Rola R, LeFevour A, Morhardt D, Curley J, Mizumatsu S, et al. Radiation-induced cognitive impairments are associated with changes in indicators of hippocampal neurogenesis. Radiat Res. 2004;162(1):39-47.

91. Rola R, Raber J, Rizk A, Otsuka S, VandenBerg SR, Morhardt DR, et al. Radiation-induced impairment of hippocampal neurogenesis is associated with cognitive deficits in young mice. Exp Neurol. 2004;188(2):316-30.

92. Boyd A, Byrne S, Middleton RJ, Banati RB, Liu GJ. Control of Neuroinflammation through Radiation-Induced Microglial Changes. Cells. 2021;10(9).

93. Kim S, Chung H, Ngoc Mai H, Nam Y, Shin SJ, Park YH, et al. Low-Dose Ionizing Radiation Modulates Microglia Phenotypes in the Models of Alzheimer's Disease. Int J Mol Sci. 2020;21(12).

94. Cuttler JM, Abdellah E, Goldberg Y, Al-Shamaa S, Symons SP, Black SE, et al. Low Doses of Ionizing Radiation as a Treatment for Alzheimer's Disease: A Pilot Study. J Alzheimers Dis. 2021;80(3):1119-28.

95. Rogers CL, Lageman SK, Fontanesi J, Wilson GD, Boling PA, Bansal S, et al. Low-Dose Whole Brain Radiation Therapy for Alzheimer's Dementia: Results From a Pilot Trial in Humans. Int J Radiat Oncol Biol Phys. 2023.

96. Reyes-Marin KE, Nunez A. Seizure susceptibility in the APP/PS1 mouse model of Alzheimer's disease and relationship with amyloid beta plaques. Brain Res. 2017;1677:93-100.

97. Hanania AN, Mainwaring W, Ghebre YT, Hanania NA, Ludwig M. Radiation-Induced Lung Injury: Assessment and Management. Chest. 2019;156(1):150-62.

98. Meziani L, Deutsch E, Mondini M. Macrophages in radiation injury: a new therapeutic target. Oncoimmunology. 2018;7(10):e1494488.

99. Su L, Dong Y, Wang Y, Wang Y, Guan B, Lu Y, et al. Potential role of senescent macrophages in radiation-induced pulmonary fibrosis. Cell Death Dis. 2021;12(6):527.

100. Teresa Pinto A, Laranjeiro Pinto M, Patricia Cardoso A, Monteiro C, Teixeira Pinto M, Filipe Maia A, et al. Ionizing radiation modulates human macrophages towards a pro-inflammatory phenotype preserving their pro-invasive and pro-angiogenic capacities. Sci Rep. 2016;6:18765.

101. Wang B, Wang H, Zhang M, Ji R, Wei J, Xin Y, et al. Radiation-induced myocardial fibrosis: Mechanisms underlying its pathogenesis and therapeutic strategies. J Cell Mol Med. 2020;24(14):7717-29.

102. Barlaz Us S, Vezir O, Yildirim M, Bayrak G, Yalin S, Balli E, et al. Protective effect of N-acetyl cysteine against radiotherapy-induced cardiac damage. Int J Radiat Biol. 2020;96(5):661-70.

103. Weintraub NL, Jones WK, Manka D. Understanding radiation-induced vascular disease. J Am Coll Cardiol. 2010;55(12):1237-9.

104. Wang Z, Jia Z, Zhou Z, Zhao X, Wang F, Zhang X, et al. Long-Term Cardiac Damage Associated With Abdominal Irradiation in Mice. Front Pharmacol. 2022;13:850735.

105. Andersen MJ, Borlaug BA. Invasive hemodynamic characterization of heart failure with preserved ejection fraction. Heart Fail Clin. 2014;10(3):435-44.

106. Farris SD, Moussavi-Harami F, Stempien-Otero A. Heart failure with preserved ejection fraction and skeletal muscle physiology. Heart Fail Rev. 2017;22(2):141-8.

107. Noll NA, Lal H, Merryman WD. Mouse Models of Heart Failure with Preserved or Reduced Ejection Fraction. Am J Pathol. 2020;190(8):1596-608.

108. Sadhu S, Decker C, Sansbury BE, Marinello M, Seyfried A, Howard J, et al. Radiation-Induced Macrophage Senescence Impairs Resolution Programs and Drives Cardiovascular Inflammation. J Immunol. 2021;207(7):1812-23.

109. Katayama I, Hotokezaka Y, Matsuyama T, Sumi T, Nakamura T. Ionizing radiation induces macrophage foam cell formation and aggregation through JNK-dependent activation of CD36 scavenger receptors. Int J Radiat Oncol Biol Phys. 2008;70(3):835-46.

110. Yang Y, Lv J, Jiang S, Ma Z, Wang D, Hu W, et al. The emerging role of Toll-like receptor 4 in myocardial inflammation. Cell Death Dis. 2016;7(5):e2234.

111. Paun A, Fox J, Balloy V, Chignard M, Qureshi ST, Haston CK. Combined Tlr2 and Tlr4 deficiency increases radiation-induced

pulmonary fibrosis in mice. Int J Radiat Oncol Biol Phys. 2010;77(4):1198-205.

112.   Su Y, Ding J, Yang F, He C, Xu Y, Zhu X, et al. The regulatory role of PDE4B in the progression of inflammatory function study. Front Pharmacol. 2022;13:982130.

113.   Lim JE, Sargur Madabushi S, Vishwasrao P, Song JY, Abdelhamid AMH, Ghimire H, et al. Total marrow irradiation reduces organ damage and enhances tissue repair with the potential to increase the targeted dose of bone marrow in both young and old mice. Front Oncol. 2022;12:1045016.

114.   Faust TE, Feinberg PA, Oa Connor C, Kawaguchi R, Chan A, Strasburger H, et al. A comparative analysis of microglial inducible Cre lines. bioRxiv. 2023.

SUPPLEMENTARY INFORMATION

Genotyping – The mice were genotyped for *Pde4b* or *App/Ps1* with PCR. The DNA was extracted from toe or ear clips at 95°C for 10 min using extraction buffer (10620, Quantabio). Next, the extracted DNA sample was added to a PCR mix containing forward, reverse, and mutant primers (**Supplementary Table 1**), Milli-Q water, KAPA2G Fast genotyping mix (07961804001, KAPA Biosystems) and, MgCl$_2$ according to manufactures protocol. The DNA was amplified using a specified PCR program (**Supplementary Table 2**), followed by loading on a 1% agarose gel containing UltraPura Agarose (16500100, Invitrogen, Waltham, MA, USA), and GelRed (1:1000; Biotium, Fremont, CA, USA) along with a 100 base pair (bp) ladder. DNA migration was induced by 100 V application on the gel for 10 min, followed by 160 V for 30 min.

Microglia isolation MACS – Primary murine microglia from P21 *Cx3cr1*$^{eGFP/+}$ were isolated according to the protocol of Bohlen *et al.* for surveillance experiments (43). Briefly, P21 pups were decapitated followed by cortices isolation and mechanical homogenization in DMEM (D6429, Sigma-Aldrich, Belgium). Next, the homogenized cortices were incubated with papain (9001-73-4, Sigma-Aldrich, Belgium) and DNase I (04536282001, Roche, Switzerland) for 30 min. The homogenate was ceived through a 70 μm cell strainer, followed by centrifugation at 500 g for 10 min at room temperature (RT). Subsequently, the cell pellet was resuspended in 30% stock isotonic percoll (SIP; 17089101, Percoll, GE Healthcare, USA) and underlaid with 70% SIP to create a density gradient.

Supplementary Table 1: Primer sequences *Pde4b* and *App/Ps1* used for genotyping mice.

Gene	Forward primer	Reverse primer	Mutant primer
Pde4b	GAGGGGAATGGAGAT TAGCC	GCCCATGAATTAAACAGCA GCAG	CTAAAGCGCATGCTCCAGACT G
App/Ps1	GTGTGATCCATTCCAT CAGC	GGATCTCTGAGGGGTCCAG T	ATGGTAGAGTAAGCGAGACG

Microglia isolation shake-off – P0-P3 *Pde4b*$^{+/+}$, *Pde4b*$^{+/-}$, or *Pde4b*$^{+/-}$ pups were decapitated and cortices were isolated, followed by meninges removal and the mechanical homogenization in Dulbecco's Modified Eagle Medium (DMEM; 041965-039, Sigma-Aldrich, Belgium). Next, the homogenate was centrifuged for 5 min at 300 g whereafter the cell pellet was resuspended in DMEM supplemented with 1% penicillin/streptomycin (P/S; 09-757F, Lonza, Switzerland) and 10% heat-inactivated fetal calf serum (FCS; 26140-79, Gibco) (DMEM 10:1). Subsequently, the mixed glial culture was maintained for seven days on flasks pre-coated with poly-L lysine (PLL, 50 μg/mL; 25988-63-0, Sigma-Aldrich), followed by seven days of incubation with DMEM 10:1 supplemented with 30% L929 conditioned medium (LCM) containing macrophage colony stimulating factor (M-CSF) to enrich the microglia population. Primary microglia were separated from the mixed glial culture by shake-off for 3 hours at 230 rpm at 37°C. Isolated microglia were then seeded at the appropriate density for each experiment. The mixed glial culture and isolated microglia were maintained at 5% CO$_2$ and 37°C.

Supplementary Table 2: PCR program for *Pde4b* and *App/Ps1* genotyping.

95°C	3 min	
95°C	15 s	
60°C	15 s	34 x
72°C	30 s	
72°C	3 min	
4°C	Infinite	

The density gradient was centrifuged at 500 g for 25 min at RT with no brake and acceleration on zero. The mononuclear cells were collected from the 70%-30% interface and washed once with 1x phosphate buffered saline (PBS), followed by centrifugation at 500 g at 4°C for 5 min. The mononuclear cells were resuspended in 1 x PBS supplemented with 2 mM EDTA and 0.5% FCS. Microglia were isolated with CD11b$^+$ magnetic beads using MACS. Microglia were seeded on poly-D-lysine (PDL; A38904-01, Gibco) and collagen (2μg/mL; 9007-34-5, Sigma-Aldrich) coated glass inserts (80826, Ibidi). Afterward, microglia were kept in culture for seven days on 10:1 DMEM followed by seven days of cultivation in DMEM F12 (D6421, Sigma-Aldrich) supplemented with 1% P/S, Na$^+$ Selenite (1:1000), insulin (1:2000), apo-transferrin (1:20), heparan-sulfate (1:1000), acetyl-cysteine

(1:1000), human TGFβ$_2$ (1:1000), cholesterol (1:1000), murine IL-34 (1:1000), and L-glutamine (1:1000) at 37°C in 5% CO_2.

qPCR – Microglia, isolated by the shake-off method, were seeded 250 000 cells/well and lysed using QIAzol Lysis Reagent (79306, Qiagen). Afterward, chloroform was added to the QIAzol mixture containing the cells, followed by incubation at RT for 2-5 min and centrifuged for 15 min at 4°C at 14 000 rpm. mRNA was isolated from the top phase and resuspended in 2-isopropanol, followed by overnight incubation at -20°C. The mRNA 2-isopropanol mixture was centrifuged for 10 min at 14 000 rpm at 4°C. Next, the RNA pellet was washed twice with cold 75% ethanol and centrifuged at 10 min for 14 000 rpm. After the pellet was dried, the mRNA was resuspended in Milli-Q water (MQ) and incubated twice for 10 min in between vortexing. The RNA concentration was determined using the Nanodrop. cDNA was obtained by adding 16 µL of RNA template with 4 µL of Qscript cDNA supermix (95048, Quantabio) following a PCR scheme (**Supplementary Table 3**). cDNA was diluted to 5 ng/µL and qPCR was initiated by adding

Supplementary Table 3: PCR program for cDNA synthesis.

25°C	5 min
42°C	30 min
85°C	5 min
4°C	Infinite

5 µL SYBR green (S7563, ThermoFisher Scientific), 1.9 µL MQ and 0.3 µL of forward and reverse primer with 2.5 µL of cDNA. The expression of phagocytosis genes *Cd36*, *Trem2*, and *Tlr4* and cAMP-specific *Pde* genes *Pde4a*, *Pde7a*, *Pde7b*, and *Pde8a* was represented as the

ΔΔCt method relative to *Pde4b$^{+/+}$* expression with the reference genes *Ywhaz* and *Cyca*. The primer sequences are presented in **Supplementary Table 4**.

Object location task – The OLT was performed in a 40 cm high arena, covered with white paper on the back and transparent in the front. All mice were habituated to the arena and all the objects by a 4 min trial for two consecutive days (**Supplementary Table 5**). Preference to either side of the arena or objects were analyzed before starting the OLT. After one resting day, the OLT was initiated. The mice were randomized for the objects and object movement (**Supplementary Table 6**). Before each trial, the mouse was placed in an empty cage for 4 min to increase exploration time. After every trial, the arena and objects were cleaned with 75% ethanol to remove olfactory clues. Mice with a total exploration time lower than 4 s were excluded in the analysis.

Spontaneous Y-maze alternation task – The Y-maze consists of three, labeled arms (A, B, and C) separated at an angle of 120°. The mouse was placed in one arm of the Y-maze, according to a randomized scheme (**Supplementary Table 7**), and was left free to explore the Y-maze for 6 min. The arm entrance was manually recorded by a blinded researcher for the experimental groups An arm entrance was considered when the hind paws of the mice entered the arm. The Y-maze was cleaned with 75% ethanol after each trial to avoid olfactory cues.

Echocardiography – The bone marrow transplantation was repeated with the same groups as before. Briefly, WT mice received bone marrow from *Pde4b$^{+/+}$* mice, while three AD groups were generated, which received bone marrow from *Pde4b$^{+/+}$*, *Pde4b$^{+/-}$*, or *Pde4b$^{-/-}$* mice.

Supplementary Table 4: Primer sequences for qPCR of primary murine microglia genes.

Gene	Forward primer	Reverse primer
Cd36	GGACATTGAGATTCTTTTCCTCTG	GCAAAGGCATTGGCTGGAAGAAC
Trem2	CTGGAACCGTGACCATCACTC	CGAAACTCGATGACTCCTCGG
Tlr4	TTTATTCAGAGCCGTTGGTG	CAGAGGATTGTCCTCCCATT
Pde4a	GCCTTGCACTGAGGAAACTC	GGCTGTCTCCTGCTTCAAAC
Pde7a	TGGAGGCTCAGATAGGTGCT	CCAGTTCCGACATGGGTTAC
Pde7b	ATCGCTTGACAAATGGGAAC	GGGTTGTGACCGTGGTAATC
Pde8a	TGGCTGTGCTCTACAACGAC	CCGGTAGTCATTCCTCTCCA
Cypa	GCCTCTCCTTCGAGCTGTT	AAGTCACCACCCTGGCA
Ywhaz	AGCCGAGCTGTCTAACCGAG	GCCAACTAGCGGTAGTAGTCA

Supplementary Table 5: Randomization scheme for both training days during the OLT. The number of mice go from 1-38 and the numbers below the training days describe objects 1, 2, 3, and 4 representing a white bottle, metal cube, brass cone, and aluminum cube with tapering top, respectively.

Mouse	Day of testing	
	1	2
1	12	34
2	23	41
3	34	12
4	41	23
5	12	34
6	23	41
7	43	21
8	14	32
9	21	43
10	32	14
11	43	21
12	14	32
13	12	34
14	23	41
15	34	12
16	41	23
17	12	34
18	23	41
19	43	21
20	14	32
21	21	43
22	32	14
23	43	21
24	14	32
25	12	34
26	23	41
27	34	12
28	41	23
29	12	34
30	23	41
31	43	21
32	14	32
33	21	43
34	32	14
35	43	21
36	14	32
37	12	34

OLT, Object Location Task

Transthoracic echocardiography was assessed 6 weeks after the bone marrow transplantation. A female WT and male AD aged-matched littermate were taken along as control. All mice were 3 months old. A Vivid*i* ultrasound machine (GE Vingmed Ultrasound) and 55 MHz probe (MX550D) were used for the echocardiography. Mice were anesthetized with 2% isoflurane and the fur of the chest was removed to ease heart visualization. The electrocardiogram leads were connected to the limbs of the mouse. The fraction shortening (FS), the cardiac output (CO), stroke volume (SV), and ejection fraction (EF) were calculated on a parasternal long-axis image mid ventricular level in B-mode. The anterior left ventricular wall thickness (AWT) and posterior left ventricular wall thickness (PWT) in diastole (d) and systole (s) were obtained from M-mode images at mid ventricular level in the short-axis view.

SUPPLEMENTARY RESULTS

Surveillance – TIC medium was used to obtain microglia with a high-order of processes and ramifications. Despite this, the microglia used for the surveillance experiments did not show this phenotype before or after treatment with DMSO (**Supplementary Figure 1.A**), roflumilast (**Supplementary Figure 1.B**), or A33 (**Supplementary Figure 1.C**). The lack of ramifications can be attributed to several factors. Firstly, mechanical homogenization could be insufficient, leading to reduced isolation of microglia. Secondly, the enzymatic homogenization with papain was inappropriate due to a new concentration of papain compared to previously used stock solutions leading to reduced cell isolation. Thirdly, 1 h coating with PDL followed by 1 h coating with collagen was demonstrated to be inadequate since gentle volume changes could already lead to the detachment of microglia.

Supplementary Table 6: Randomization scheme for the OLT. The number of mice go from 1-38 and the numbers below the days describe objects 1, 2, 3, and 4 representing a white bottle, metal cube, brass cone, and aluminum cube with tapering top, respectively. F and B indicate movement of the object to the front, or back, respectively during trial 2.

Mouse	Day of testing															
	1		2		3		4		5		6		7		8	
1	11	1F	22	B2	33	3B	44	F4	33	B3	44	4F	11	F1	22	2B
2	22	2F	33	B3	44	4B	11	F1	44	B4	11	1F	22	F2	33	3B
3	33	3F	44	B4	11	1B	22	F2	11	B1	22	2F	33	F3	44	4B
4	44	4B	11	F1	22	2F	33	B3	22	F2	33	3B	44	B4	11	1F
5	11	1B	22	F2	33	3F	44	B4	33	F3	44	4B	11	B1	22	2F

6	22	2B	33	F3	44	4F	11	B1	44	F4	11	1B	22	B2	33	3F
7	33	F3	44	4B	11	B1	22	2F	11	1B	22	F2	33	3F	44	B4
8	44	F4	11	1B	22	B2	33	3F	22	2B	33	F3	44	4F	11	B1
9	11	F1	22	2B	33	B3	44	4F	33	3B	44	F4	11	1F	22	B2
10	22	B2	33	3F	44	F4	11	1B	44	4F	11	B1	22	2B	33	F3
11	33	B3	44	4F	11	F1	22	2B	11	1F	22	B2	33	3B	44	F4
12	44	B4	11	1F	22	F2	33	3B	22	2F	33	B3	44	4B	11	F1
13	11	1F	22	B2	33	3B	44	F4	33	B3	44	4F	11	F1	22	2B
14	22	2F	33	B3	44	4B	11	F1	44	B4	11	1F	22	F2	33	3B
15	33	3F	44	B4	11	1B	22	F2	11	B1	22	2F	33	F3	44	4B
16	44	4B	11	F1	22	2F	33	B3	22	F2	33	3B	44	B4	11	1F
17	11	1B	22	F2	33	3F	44	B4	33	F3	44	4B	11	B1	22	2F
18	22	2B	33	F3	44	4F	11	B1	44	F4	11	1B	22	B2	33	3F
19	33	F3	44	4B	11	B1	22	2F	11	1B	22	F2	33	3F	44	B4
20	44	F4	11	1B	22	B2	33	3F	22	2B	33	F3	44	4F	11	B1
21	11	F1	22	2B	33	B3	44	4F	33	3B	44	F4	11	1F	22	B2
22	22	B2	33	3F	44	F4	11	1B	44	4F	11	B1	22	2B	33	F3
23	33	B3	44	4F	11	F1	22	2B	11	1F	22	B2	33	3B	44	F4
24	44	B4	11	1F	22	F2	33	3B	22	2F	33	B3	44	4B	11	F1
25	11	1F	22	B2	33	3B	44	F4	33	B3	44	4F	11	F1	22	2B
26	22	2F	33	B3	44	4B	11	F1	44	B4	11	1F	22	F2	33	3B
27	33	3F	44	B4	11	1B	22	F2	11	B1	22	2F	33	F3	44	4B
28	44	4B	11	F1	22	2F	33	B3	22	F2	33	3B	44	B4	11	1F
29	11	1B	22	F2	33	3F	44	B4	33	F3	44	4B	11	B1	22	2F
30	22	2B	33	F3	44	4F	11	B1	44	F4	11	1B	22	B2	33	3F
31	33	F3	44	4B	11	B1	22	2F	11	1B	22	F2	33	3F	44	B4
32	44	F4	11	1B	22	B2	33	3F	22	2B	33	F3	44	4F	11	B1
33	11	F1	22	2B	33	B3	44	4F	33	3B	44	F4	11	1F	22	B2
34	22	B2	33	3F	44	F4	11	1B	44	4F	11	B1	22	2B	33	F3
35	33	B3	44	4F	11	F1	22	2B	11	1F	22	B2	33	3B	44	F4
36	44	B4	11	1F	22	F2	33	3B	22	2F	33	B3	44	4B	11	F1
37	11	1F	22	B2	33	3B	44	F4	33	B3	44	4F	11	F1	22	2B
38	22	2F	33	B3	44	4B	11	F1	44	B4	11	1F	22	F2	33	3B

OLT, Object Location task.

Supplementary Table 7: Randomization scheme arm entrance Y-maze.

| Mouse	Start arm
1	A
2	B
3	C
4	A
5	B
6	C
7	A
8	B
9	C
10	A
11	B
12	C
13	A
14	B
15	C
16	A
17	B
18	C
19	A
20	B
21	C
22	A
23	B
24	C
25	A
26	B
27	C
28	A
29	B
30	C
31	A

32	B
33	C
34	A
35	B
36	C
37	A
38	B

These aforementioned problems already led to the sparse amount of microglia that could be seeded, while dense cultivation of microglia is needed to obtain healthy microglia. These problems are tackled in future experiments by 1) prolonged mechanical dissociation of the brains, 2) adjustment of the papain depending on the number of brains used, and 3) PDL and collagen will be diluted in 1x PBS instead of MQ.

Phagocytosis confluence – The phagocytic index was measured by dividing the area covered by pHrodo positive signal by the area covered by cells (**Figure 3.D**). Therefore, differences in cell confluence over time and between *Pde4b* conditions were investigated since alternations in the confluence between the experimental conditions influence the phagocytic index. The confluence did significantly differ between 1 h after synaptosome administration and 24 h after synaptosome administration in each group. However, the area covered by cells was stable between each other time points (**Supplementary Figure 3.A**). This difference between 1 and 24 h after synaptosome administration can potentially be explained by a higher degree of microglial processes needed for phagocytosis upon synaptosome phagocytosis rather than increased proliferation of the microglia. The cell area was not significantly different between *Pde4b*$^{+/+}$, *Pde4b*$^{+/-}$, or *Pde4b*$^{-/-}$ microglia at each time point (**Supplementary Figure 3.B**). Therefore, differences in the phagocytic index can not be attributed to differences in the confluence between the *Pde4b* genotypes.

Location and object preference during OLT – An OLT was executed to assess the effect of microglial-specific *Pde4b* expression on cognitive decline in the murine APP/PS1 model of AD. The OLT arena was tested for left-right preference and object preference to exclude the interference of the arena environment with the obtained test results. The mice displayed no preference to the left or right object, indicating no arena side preference (**Supplementary Figure 2.A**).
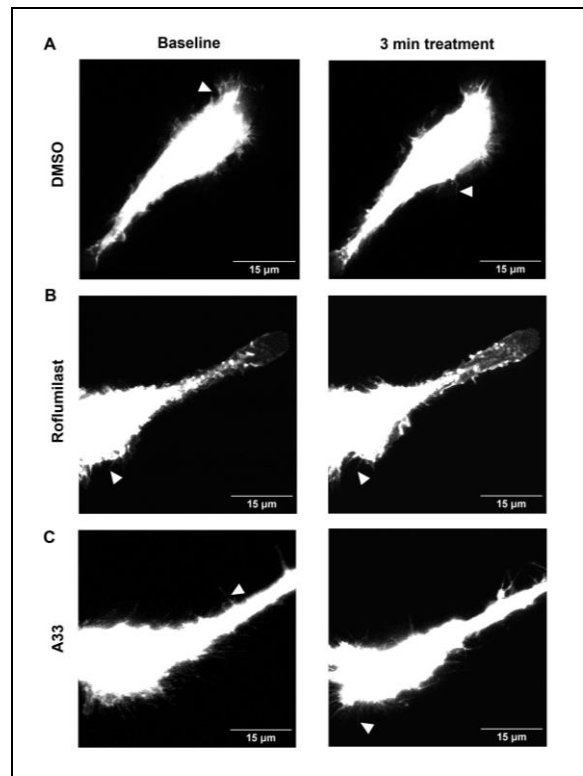

Supplementary Figure 1: Highly ramified microglia were not obtained after TIC medium incubation but filopodia were visible. (A, B, and C) Representative pictures of microglia during baseline or after 3 min of treatment with (A) 0.05% DMSO, (C) 3 nM roflumilast or (E) 100 nM A33 with the white arrowhead indicating filopodia. Scale bar = 15 μm.

An object preference was observed for object 4 (aluminum cube with tapering on top) compared to object 3 (brass cone) (**Supplementary Figure 2.B**). Despite this, the preference in objects does not interfere with the OLT since two similar objects are always placed in the arena.
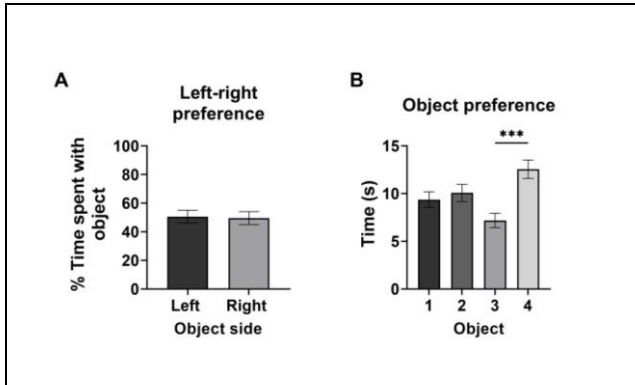
Supplementary Figure 2: APP/PS1 mice with microglia-specific *Pde4b* expression showed no left-right preference in the OLT arena but did demonstrate object preference. (A) Left-right preference in the OLT arena was measured with the percentage (%) of time spent with the left or right object. (B) Object preference is represented as the time (s) spent with each object 1, 2, 3, and 4 representing a white bottle, metal cube, brass cone, and aluminum cube with tapering top, respectively. (A, B) Both preference tests were conducted during two consecutive training days. Data are represented as mean ± SEM, analyzed with (A) a two-sided t-test and (B) a one-way ANOVA corrected for multiple comparisons, with Tukey's correction ***p<0.001.
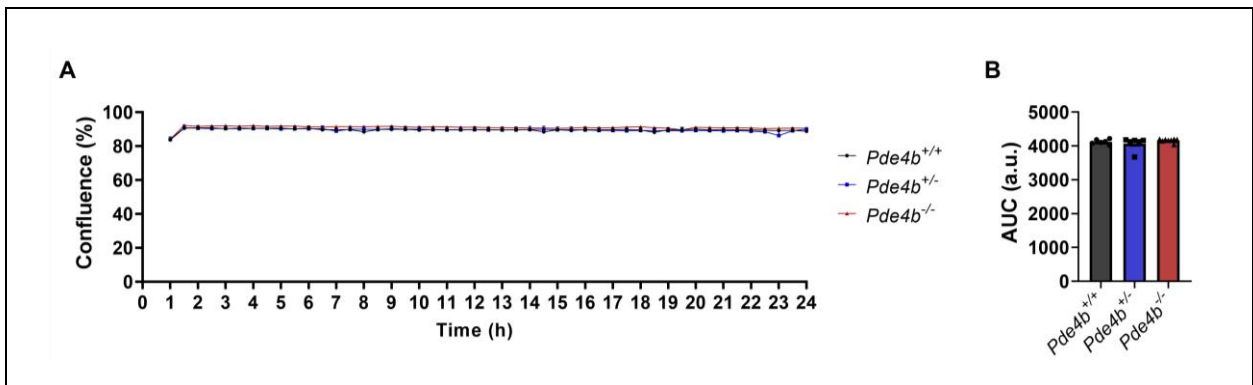
Supplementary Figure 3: Confluence of primary murine microglia was lower at baseline compared to 24 h after synaptosome administration but did not differ between *Pde4b* genotypes. (A) Confluence of *Pde4b*$^{+/+}$, *Pde4b*$^{+/-}$, or *Pde4b*$^{-/-}$ primary murine microglia was measured as the area covered by cells during live-cell synaptosome phagocytosis of pHrodo-labeled synaptosomes. (B) The area under the curve did not differ between *Pde4b*$^{+/+}$, *Pde4b*$^{+/-}$, or *Pde4b*$^{-/-}$ conditions. Data are represented as mean ± SEM and n=6-8 per group. AUC, area under the curve; a.u., arbitrary unit.